A quantitative gibberellin signalling biosensor reveals a role for gibberellins in internode specification at the shoot apical meristem

Bihai Shi[1*], Amelia Felipo-Benavent[2*], Guillaume Cerutti[1], Carlos Galvan-Ampudia[1], Lucas Jilli[2], Geraldine Brunoud[1], Jérome Mutterer[2], Lali Sakvarelidze-Achard[2], Jean-Michel Davière[2], Alejandro Navarro-Galiano[3], Ankit Walia[4], Shani Lazary[5], Jonathan Legrand[1], Roy Weinstein[5], Alexander M. Jones[4], Salomé Prat[3], Patrick Achard[2†], Teva Vernoux[1†]

[1] Laboratoire Reproduction et Développement des Plantes, Univ Lyon, ENS de Lyon, CNRS, INRAE, INRIA, F-69342, Lyon, France

[2] Institut de biologie moléculaire des plantes, CNRS, Université de Strasbourg, 67084 Strasbourg, France

[3] Centre for Research in Agricultural Genomics, 08193 Cerdanyola, Barcelona, Spain

[4] Sainsbury Laboratory, Cambridge University, Cambridge CB2 1LR, United Kingdom

[5] Department of Molecular Biology and Ecology of Plants, Tel Aviv University, Tel Aviv 69978, Israel

[*]These authors contributed equally

[†]To whom correspondence should be addressed: T.V. (teva.vernoux@ens-lyon.fr) or P.A. (patrick.achard@ibmp-cnrs.unistra.fr)

Abstract

Growth at the shoot apical meristem (SAM) is essential for shoot architecture construction. The phytohormones gibberellins (GA) play a pivotal role in coordinating plant growth, but their role in the SAM remains mostly unknown. Here, we developed a ratiometric GA signalling biosensor by engineering one of the DELLA repressors, to suppress its master regulatory function in GA transcriptional responses while preserving its degradation upon GA sensing. We demonstrate that this novel degradation-based biosensor accurately reports on cellular changes in GA levels and perception during development. We used this biosensor to map GA signalling activity in the SAM. We show that high GA signalling is found primarily in cells located between organ primordia that are the precursors of internodes. By gain- and loss-of-function approaches, we further demonstrate that GAs regulate cell division plane orientation to establish the typical cellular organisation of internodes, thus contributing to internode specification in the SAM.

Introduction

The shoot apical meristem (SAM) at the tip of shoot axes comprises a stem cell niche whose activity produces lateral organs and stem segments in a modular iterative fashion during the whole plant life. Each of these repetitive units or phytomere includes an internode and lateral organs at a node and an axillary meristem at the leaf axil[1]. The growth and organization of phytomeres change during development. In *Arabidopsis thaliana*, internode growth is inhibited during the vegetative phase and axillary meristems rest dormant at the axils of rosette leaves. Upon floral transition, the SAM turns into an inflorescence meristem, producing elongated internodes and axillary buds that form branches at the axils of cauline leaves, and later flowers without leaves[2]. While substantial progress has been made on our understanding of the mechanisms controlling the initiation of leaves, flowers and branches, much less is known on how internodes are initiated.

Growth via cell division and expansion is essential for reiterative organogenesis at the SAM. The tetracyclic diterpenoid hormones gibberellins (GA) are key growth regulators[3–5], with a crucial role in many embryonic and post-embryonic developmental processes[6]. Central to the GA signalling pathway are the five DELLA proteins, GIBBERELLIC ACID INSENSITIVE (GAI), REPRESSOR OF GA1-3 (RGA) and (RGL) RGA-Like 1-3[7]. These nuclear proteins are composed of an N-terminal DELLA/TVHYNP domain and of a GRAS domain. The GRAS domain allows DELLAs to interact with diverse target transcription factors and transcriptional regulators and to suppress growth by modulating their activity[7]. Binding of GA to the GIBBERELLIN INSENSITIVE DWARF1 (GID1) GA receptor promotes GID1 interaction with the N-terminal domain of DELLAs, triggering DELLA degradation by the ubiquitin-dependent proteasome pathway[7–10], and in turn, de-repressing GA responses. Despite the relatively specialised role of the GRAS and DELLA/TVHYNP domains, residues

60 required for DELLA degradation and partner protein interaction are widely distributed within
61 the protein sequence.
62 The identification of genes encoding GA catabolic enzymes as direct targets of the class I
63 KNOX meristem identity regulators has led to propose that GA levels are low in the SAM
64 cells, while high GA concentrations trigger growth of lateral organs[3–5]. Low GA levels could
65 then contribute to SAM maintenance[3]. However, more recent analysis indicate also that GAs
66 promote the increase in SAM size during floral transition by regulating the division and
67 expansion of inner SAM cells[11,12], in a similar manner as in the root[13,14]. DELLAs were
68 likewise found to limit meristem size by directly regulating the expression of the cell-cycle
69 inhibitor KRP2 in the internal part of the SAM (the rib zone)[12]. Together, these findings
70 support a role for GA in positively regulating cell division in the inner tissues of the SAM,
71 and thus SAM size. At the same time, several genes encoding GA biosynthetic and
72 degradation enzymes are expressed specifically in lateral organs[4,11], illustrating a complex
73 spatio-temporal GA distribution in the SAM to likely fulfil different functions.
74 Accessing spatio-temporal GA distribution has been instrumental to better understand
75 function of these hormones in different tissues and at various developmental stages.
76 Accumulation of GA in the root endodermis and regulation of their cellular level via GA
77 transport were discovered by using bioactive fluorescein (Fl)-tagged GA[15,16]. More recently,
78 the nlsGPS1 GA FRET sensor revealed that GA levels are correlated with cell elongation in
79 roots, stamen filaments and dark-grown hypocotyls[17]. Here, building on the knowledge on the
80 GA signalling pathway, we report on the engineering and characterization of a quantitative
81 degradation-based GA signalling biosensor. We used this novel biosensor, in conjunction
82 with GA-Fls and nlsGPS1, to map the spatio-temporal distribution of GA signalling activity
83 and to quantitatively analyse how GAs regulate cell behaviour in the SAM epidermis. We

demonstrate that GAs control the orientation of division planes of SAM cells located between organ primordia, therefore specifying the typical cellular organization of internodes.

Results

Modifying the RGA protein for sensor construction (Fig. 1; Extended Data Fig. 1, 2)

To generate a degradation-based GA signalling biosensor, we engineered a DELLA protein to meet two criteria, (i) a specific degradation upon GA perception; and (ii) a minimal interference with GA signalling. To do so, we modified DELLAs to preserve the interaction with GID1 while abolishing interactions with partner transcription factors, by introducing mutations in the GRAS domain. Among the 5 *Arabidopsis* DELLAs, RGA displays one of the highest GA-dependent degradation rate[18], and RGA-GFP fusions are widely used as GA signalling reporter[8]. Leveraging on the results of GRAS domain mutant analyses in rice[19] and *Arabidopsis*[20,21](Fig. 1a, Extended Data Fig. 1a), we generated four modified RGA versions (RGA^{m1} to RGA^{m4}) and tested their ability to meet the above defined criteria (Extended Data Fig. 1). We first used a yeast-two hybrid (Y2H) assay to test the binding capacity of these modified candidates with three well known DELLA interacting partners, JAZ1, TCP14 and IDD2[22]. While RGA^{m1} had a minor effect on interactions, RGA^{m2}, RGA^{m3} and RGA^{m4} lost their capacity to interact with these partners (Fig. 1b, Extended Data Fig. 1b). In addition, RGA^{m2}, RGA^{m3} and RGA^{m4} were able to bind GID1 in the presence of GA, thus suggesting that these DELLA candidates are still degraded in response to GA (Fig. 1c, Extended Data Fig. 1c). To assess this possibility, we explored GA-dependent degradation of RGA^{m2}, RGA^{m3} and RGA^{m4} fused to GFP in transient expression assays. These three candidates were degraded after GA treatment (Fig. 1d, Extended Data Fig. 1d), RGA^{m2}-GFP having the fastest degradation kinetics although it was slightly more stable than RGA-GFP. Noteworthy, RGA^{m2} harbours three amino acid substitutions in the GRAS PFYRE motif (Fig. 1a), that is

highly conserved in all plant DELLAs. Therefore, this variant is likely to have similar properties in plant species other than *Arabidopsis*.

Based on the above results, we selected RGA^{m2} for further analysis. We next showed that RGA^{m2} is unable to bind with the BZR1 DELLA interacting partner in yeast and a larger screen confirmed that these mutations abolishes interactions with practically all known DELLA partners (Fig. 1b, Extended Data Fig. 2). Moreover, co-immunoprecipitation studies demonstrated that binding of RGA^{m2} to IDD2 is also strongly reduced *in planta* compared to RGA (Fig. 1e). Finally, transient expression assays confirmed that, while RGA represses BZR1 and TCP14 transcriptional activities, RGA^{m2} did not (Fig. 1f-g). Taken together, these data indicate that the expression of RGA^{m2} (hereafter named RGA^{mPFYR}) in plants has a negligible impact on GA signalling. Thus, RGA^{mPFYR} constitutes a suitable DELLA variant form for engineering a degradation-based biosensor that monitors GA signalling activity and more specifically the combinatorial effect of GA and of its complex perception machinery.

Engineering a GA signalling sensor (Fig. 2; Extended Data Fig. 3-5)

To create a ratiometric GA signalling sensor, we fused the RGA^{mPFYR} protein to the fast maturing yellow fluorescent protein VENUS[23] and co-expressed this fusion protein together with a nuclear-localized non-degradable reference protein, TagBFP-NLS, under the *pUBQ10*[24] or *pRPS5a*[25,26] constitutive promoter. We used the 2A self-cleaving peptide to allow for a stoichiometric production of both fluorescent proteins, enabling quantification of GA signalling activity using fluorescence intensity ratio between RGA^{mPFYR}-VENUS and TagBFP[27,28] (Fig. 2a). We named the sensor lines $qRGA^{mPFYR}$ (quantitative $\underline{RGA^{mPFYR}}$) and first analysed their TagBFP fluorescence pattern in vegetative and reproductive tissues (Fig. 2b and Extended Data Fig. 3). TagBFP fluorescence of *pUBQ10::qRGA*^{mPFYR} lines was homogeneously distributed in hypocotyl, the vegetative shoot meristem, cotyledons and roots

134 (except in the root tip) but the TagBFP signal was unevenly distributed in the inflorescence
135 SAM, with a stronger signal in organ boundaries (Extended Data Fig. 3b). Conversely, the
136 TagBFP signal was strong in the root tip and the vegetative SAM in *pRPS5a::RGA*^{mPFYR} lines
137 (Fig. 2b), and showed a homogenous distribution in the inflorescence SAM (Extended Data
138 Fig. 3e). Hence, the choice of one of these constructs depends on the analysed tissue: we used
139 *pUBQ10::RGA*^{mPFYR} in subsequent experiments in seedlings, and *pRPS5a::RGA*^{mPFYR} for
140 experiments performed in inflorescence SAM .
141 To validate that qRGA^{mPFYR} can detect changes in GA levels or signalling activity, we next
142 investigated the effects of exogenous GA and paclobutrazol (PAC; an inhibitor of GA
143 biosynthesis) treatments. Noteworthy, the growth of qRGA^{mPFYR} seedling hypocotyls was
144 similar to wild-type under mock conditions and upon GA or PAC treatment, although
145 hypocotyls were slightly longer after GA treatment (Fig. 2c). Furthermore, shoot development
146 and plant fertility were not significantly affected in qRGA^{mPFYR} plants (Fig. 2d and Extended
147 Data Fig. 3g), confirming that qRGA^{mPFYR} negligibly interferes with plant growth and GA
148 responses. Also, while the TagBFP signal was unaffected in hypocotyls upon GA and PAC
149 application, RGA^{mPFYR}-VENUS fluorescence was respectively reduced and increased after
150 these treatments, alike the *pRGA::GFP-RGA* positive control (Fig. 2e). Similar results were
151 observed in qRGA^{mPFYR} roots. In contrast, VENUS fluorescence did not change in any of the
152 treatments in RGA^{m3}-VENUS and RGA^{m4}-VENUS lines, consistently with the lower GA-
153 dependent degradation rate of these variants (Extended Data Fig. 4). In further image analyses,
154 in order to fully cover the range of values in VENUS/TagBFP fluorescence ratio, we used 3 -
155 RGA^{mPFYR}-Venus/TagBFP as a quantitative measure of GA signalling activity (hereafter
156 named "GA signalling"; Fig. 2a; see also Supplementary Method 1). This quantitative
157 approach confirmed statistically significant changes in GA signalling activity in hypocotyls,
158 with an increase and decrease respectively upon GA and PAC treatments compared to

159 untreated seedlings (Fig. 2e,f). Exogenous GA and PAC treatments induced similar responses
160 in the SAM, although the effect of PAC was less pronounced than in hypocotyl (Extended
161 data Fig. 3h-y). Furthermore, GA signalling activity increased in the SAM with both
162 exogenous GA concentration and treatment duration (Extended Data Fig. 5), showing that
163 $qRGA^{mPFYR}$ is also suitable to be used as a GA signalling sensor in the SAM.
164 Next, we tested if $qRGA^{mPFYR}$ is able to report for changes in endogenous GA levels in
165 growing hypocotyls. Hypocotyl elongation is widely used to study the effect of light and dark
166 on cell expansion, a growth process that requires GA signalling[17,29]. While in dark-grown
167 hypocotyls, cells elongate along an oriented spatio-temporal gradient (from the base to the tip),
168 in the light, hypocotyl cells elongate rather homogenously and continuously during the entire
169 growth period[30]. Thus, we investigated GA signalling distribution in $qRGA^{mPFYR}$ hypocotyls
170 grown in light and dark conditions, and concomitantly measured hypocotyl lengths from 2
171 days after sowing (DAS). Whereas at 3 DAS, hypocotyl lengths of light and dark-grown
172 seedlings were similar, dark-grown hypocotyls were substantially longer than that of light-
173 grown hypocotyls from 4 DAS and reached a plateau at 7 DAS (Fig. 2g). This growth
174 response was identical to wild type (Col-0) (Fig. 2g). We then compared GA signalling
175 activity in the basal region of light- and dark-grown $qRGA^{mPFYR}$ hypocotyls at 3, 5, and 7
176 DAS (Fig. 2h). Consistent with the growth dynamics, GA signalling was not statistically
177 different between dark- and light-grown seedlings at 3 DAS. However, at 5 DAS, GA
178 signalling activity was significantly higher in the dark than in the light, mirroring the
179 activation of cell expansion in darkness. At 7 DAS, a shift in the GA response occurred, with
180 GA signalling activity being lower in the dark than in the light, which correlates with the
181 completion of hypocotyl elongation in dark condition. Thus, $qRGA^{mPFYR}$ allows following
182 dynamic changes in GA signalling activity in growing hypocotyls.
183

qRGA^{mPFYR} fluorescence depends on GA receptor activity (Fig. 3 and Extended Data Fig. 6)

As GA signalling activity depends on both GA concentration and GA perception, we analysed the expression of the three *GID1* receptors in vegetative and reproductive tissues. In seedlings, GID1-GUS reporter lines showed that *GID1a* and *c* are highly expressed in cotyledons (Fig. 3a-c). Moreover, all three receptors are expressed in leaves, lateral root primordia, root tip (excluding root cap for *GID1b*) and vasculature (Fig. 3a-c). In the SAM, we only detected a GUS signal for GID1b and 1c (Extended data Fig. 6a-c). *In situ* hybridization confirmed these expression patterns and further demonstrated that *GID1c* is homogenously expressed at a low level in the SAM while *GID1b* shows higher expression at the SAM periphery (Extended data Fig. 6d-l). A *pGID1b::2xmTQ2-GID1b* translational fusion further revealed a graded *GID1b* expression ranging from low or no expression in the SAM centre to high expression in organ boundaries (Extended data Fig. 6m). Thus, GID1 receptors are unevenly distributed across and within tissues. Moreover, we observed that overexpressing *GID1* (*pUBQ10::GID1a-mCherry*) enhanced qRGA^{mPFYR} sensitivity to external GA application in hypocotyls (Fig. 3d). Taken together, these results suggest that differential expression of GID1 receptors can modulate qRGA^{mPFYR} emission ratio, confirming that this biosensor reports for the combinatorial action of GA and GA receptors.

A GA signalling map in the shoot apical meristem (Fig. 4; Extended Data Fig. 7-9)

Distribution of GA signalling within the SAM has remained elusive so far. Thus, we used plants expressing qRGA^{mPFYR} together with the *pCLV3::mCherry-NLS* stem cell reporter to compute a high-resolution quantitative map of GA signalling activity, focusing on the L1 layer (epidermis; Fig. 4a-b, see Methods and Supplementary Method 1) given the key role of L1 in controlling growth at the SAM[31]. Here, expression of *pCLV3::mCherry-NLS* provided a

209 fixed geometric reference for analysing the spatio-temporal distribution of GA signalling
210 activity[32]. Although GAs were proposed to be required for lateral organ development[4], we
211 observed that GA signalling was lower in flower primordia (P) from the P_3 stage onward (Fig.
212 4a-b), while young P_1 and P_2 primordia had intermediate activity similar to the one found in
213 the central zone (Fig. 4a-b). Higher GA signalling activity was found in the boundaries of
214 organ primordia, starting from P_1/P_2 (on the lateral sides of the boundary) and culminating
215 from P_4, and in all peripheral zone cells located between primordia (Fig. 4a-b; Extended data
216 Fig. 7a-b). This higher GA signalling activity was not only monitored in the epidermis, but
217 also in the L2 and upper L3 layers (Extended data Fig. 7b). This reveals a GA signalling
218 pattern mostly mirroring primordia distribution. The inter-primordia region (IPR) distribution
219 results from the progressive establishment of a high GA signalling activity between
220 developing primordia and the central zone, while in parallel GA signalling activity decreases
221 in primordia (Fig. 4c-d).
222 The distribution of GID1b and GID1c receptors (Extended Data Fig. 6b-c, g-m) suggests that
223 differential expression of GA receptors contributes to shape the GA signalling activity pattern
224 in the SAM. We wondered if differential accumulation of GA could also be involved. To
225 investigate this possibility, we used the nlsGPS1 GA FRET sensor[17]. An increased emission
226 ratio was detected in nlsGPS1 SAMs treated with 10 μM GA_{4+7} for 100 min (Extended Data
227 Fig. 8), indicating that nlsGPS1 responds to changes in GA concentration in the SAM as it
228 does in roots[17]. The spatial distribution of the nlsGPS1 emission ratio indicates that GA levels
229 are relatively low in the SAM external layers, but it shows they are elevated in the centre of
230 the SAM and in the inter-primordia region (Fig. 4e, Extended Data Fig. 8a, c). We also
231 treated SAMs with fluorescent GAs (GA_3-, GA_4-, GA_7-Fl) or with Fl alone as a negative
232 control. The Fl signal was distributed in the whole SAM, including the central zone and
233 primordia, although with lower fluorescence (Fig. 4f, Extended Data Fig. 9d). In contrast, all

the three GA-Fls specifically accumulated in primordia boundaries and also, to different degrees, in the rest of the IPR with GA_7-Fl accumulating in most IPR cells (Fig. 4g, Extended Data Fig. 9). Fluorescence intensity quantification demonstrated higher IPR cells to non-IPR cells intensity ratios in the GA-Fl treated SAMs, compared to Fl-treated SAMs (Fig. 4h, Extended Data Fig. 9c). Taken together, these results suggest that GAs are present at higher levels in IPR cells. This indicates that the SAM GA signalling activity pattern results from both differential expression of the GA receptors and from the differential accumulation of GA in IPR cells. Our analysis thus identifies an unexpected spatio-temporal GA signalling pattern, with a lower activity in the centre of the SAM and in primordia, while activity is elevated in the IPR of the peripheral zone.

Correlation analyses suggest a role for GA signalling in cell division plane orientation in the shoot apical meristem (Fig. 5)

To understand the role of differential GA signalling activity at the SAM, we analysed the correlation between GA signalling activity, cell expansion and cell division using time-lapse live imaging of qRGA^{mPFYR} *pCLV3::mCherry-NLS* SAMs. Given the role of GA in growth regulation, a positive correlation was expected with cell expansion parameters. We thus first compared maps of GA signalling activity to those of cell surfacic growth rate (as a proxy for cell expansion intensity for a given cell and daughter cells if it divides) and growth anisotropy, which measures the directionality of cell expansion (here also for a given cell and daughter cells if it divides; Fig. 5a-b, see Methods and Supplementary Method 1). Our cell surfacic growth intensity map of the SAM was consistent with previous observations[33,34], with a minimal growth rate in boundaries and maximal rates in developing flowers (Fig. 5a). A principal component analysis (PCA) showed an anti-correlation between GA signalling activity and cell surfacic growth intensity (Fig. 5c). It further showed that the main axis of

259 variability, encompassing GA signalling input and growth intensity, is orthogonal to the
260 direction defined by high expression of *CLV3*, which argues in favour of excluding cells from
261 the centre of the SAM in the rest of the analysis. Spearman correlation analyses confirmed the
262 PCA results (Fig. 5d), suggesting that higher GA signalling in the IPR does not lead to cell
263 expansion. However, the correlation analysis demonstrated a mild positive association
264 between GA signalling activity and growth anisotropy (Fig. 5c,d), suggesting that higher GA
265 signalling in the IPR act on cell growth orientation and possibly cell division plane
266 positioning.
267 Thus, we next studied the correlation between GA signalling and cell division activity, by
268 identifying newly formed cell walls during a time course analysis (Fig. 5e). This methodology
269 allows us to measure both the frequency and orientation of cell divisions. Strikingly, we found
270 that cell division frequency was similar in the IPR and the rest of the SAM (non-IPR, Fig. 5f),
271 showing that differences in GA signalling between IPR and non-IPR cells do not have a major
272 effect on cell division. This, together with the positive correlation between GA signalling and
273 growth anisotropy, lead us to ask whether GA signalling activity could act on cell division
274 plane orientation. We measured the orientation of new cell walls as the angle relative to the
275 radial axis connecting the centre of the meristem to the centre of the new cell walls (Fig. 5g),
276 and observed that cells had a clear tendency to divide at angles closer to 90° relative to the
277 radial axis, with the highest frequency observed at 70-80° (23.28%) and 80-90° (22.62%) (Fig.
278 5h) i.e. corresponding to cell divisions oriented in the circumferential/transverse direction. To
279 explore the contribution of GA signalling to this cell division behaviour, we analysed
280 separately the cell division parameters in the IPR and in the rest of the SAM (Fig. 5h). We
281 observed that the angle of cell division was different in the IPR compared to the rest of SAM
282 cells (non-IPR) or the entire SAM (Fig. 5h); IPR cells showing a higher rate of transverse cell
283 divisions, i.e. 70-80° and 80-90° (33.86% and 30.71% respectively) (Fig. 5h). Thus, our

observations reveal a link between high GA signalling and cell division plane orientation, that parallels the correlation between GA signalling activity and growth anisotropy (Fig. 5c,d). To further establish spatial conservation of this link, we measured the orientation of division planes in IPR cells above primordia starting at stage P_3, given that the highest GA signalling activity is detected in this region from stage P_4 (Fig. 4). The division angles of the IPR above P_3 and P_4 did not show statistically significant differences, although an increase in the frequency of transverse cell divisions was observed in the IPR above P_4 (Fig. 5i). Differences in cell division plane orientation were however statistically significant in IPR cells above P_5, in which the frequency of transverse cell divisions was drastically increased (Fig. 5i). Taken together, these results suggest that GA signalling controls orientation of cell division in the SAM coherently with previous reports[35,36], high GA signalling likely inducing a transverse orientation of cell divisions in the IPR.

GA signalling activity positively regulates transverse cell divisions in the shoot apical meristem (Fig. 6; Extended Data Fig. 10-12)

Cells in the IPR are expected not to be incorporated into primordia but rather in the internodes[2,37,38]. A transverse orientation of cell divisions in the IPR could generate the typical organization in parallel longitudinal cell files of the internode epidermis. Our observations above indicate that GA signalling is likely to act in this process by regulating cell division orientation.

Loss-of-function of multiple *DELLA* genes leads to constitutive GA response and thus *della* mutants could be used to test this hypothesis[39]. We first analysed the expression patterns of the five *DELLA* genes in the SAM. Transcriptional fusion GUS lines[40] showed that *GAI, RGA,* and *RGL1* are expressed in the SAM and to a much lesser extent, *RGL2* (Extended Data Fig. 10a-d). *In situ* hybridization further showed that *GAI* mRNA specifically accumulates in

primordia and developing flowers (Extended Data Fig. 10e). *RGL1* and *RGL3* mRNA were detected throughout the SAM dome and in older flowers, while *RGL2* mRNA was more abundant in the boundary regions (Extended Data Fig. 10f-h). Confocal imaging of *pRGL3::RGL3-GFP* SAM confirmed the expression observed with *in situ* hybridization and showed that the RGL3 protein accumulates in the central part of the SAM (Extended Data Fig. 10i). Using a *pRGA::GFP-RGA* line, we also found that the RGA protein accumulates in the SAM, but its abundance is reduced in boundaries starting from P_4 (Extended Data Fig. 10j). Notably, the expression patterns of *RGL3* and *RGA* are compatible with a higher GA signalling activity in the IPR, as detected with $qRGA^{mPFYR}$ (Fig. 4). In addition, these data indicate that all *DELLAs* are expressed in the SAM and that collectively, their expression covers the entire SAM.

We next analysed the cell division parameters in wild-type (L*er*, control) and quintuple (global) *gai-t6 rga-t2 rgl1-1 rgl2-1 rgl3-4 della* mutants (Fig. 6a-b). Interestingly, we observed a statistically significant change in frequency distribution of cell division angles in the SAM of global *della* mutant compared to wild-type (Fig. 6c). This change in the global *della* mutant resulted from an increase in frequency of 80-90° angles (34.71 % vs 24.55 %) and to a lesser extent of 70-80° angles (23.78 % vs 20.18 %), i.e. corresponding to transverse cell divisions (Fig. 6c). The frequency of non-transverse divisions (0-60°) was also lower in global *della* mutant (Fig. 6c). The increased occurrence of transverse cell divisions was easily visible in the SAM of global *della* mutant (Fig. 6b). The frequency of transverse cell divisions in the IPR was also higher in global *della* mutant compared to wild-type (Fig. 6d). Outside of the IPR region, distribution of the angle of cell division was more homogeneous in wild-type, while in the global *della* mutant it was skewed toward tangential divisions, as in the IPR (Fig. 6e). Collectively, these observations indicate that constitutive activation of GA signalling in the SAM induces transverse cell division both in the IPR and the rest of the SAM.

The orientation of cell division has been proposed to be influenced by the geometry of the SAM and notably by tensile stresses prescribed by the curvature of the tissue[41]. We thus analysed the SAM shape of the global *della* mutant. As previously shown[12], the size of the global *della* mutant SAM was bigger than wild-type (Extended Data Fig. 11a,b,d). However, the SAM curvature was identical in the two genotypes (Extended Data Fig. 11b,e,f,g,h,j). We observed a comparable increase in size in the quadruple *gai-t6 rga-t2 rgl1-1 rgl2-1 della* mutant, again without modification of the curvature compared to wild-type (Extended Data Fig. 11c,d,f,i,j). Frequency of cell division orientation was also affected in the quadruple *della* mutant, but to a lesser extent than in the global *della* mutant (Extended Data Fig. 12). This dosage effect, along with the absence of effects on curvature, suggests that changes in the occurrence of transverse cell division depends on changes in GA signalling activity rather than in SAM geometry, and that the remaining RGL3 activity in quadruple *della* mutants limits the change in cell division orientation caused by the loss of DELLA activity. Taken together, our results indicate that GA signalling positively regulates transverse orientation of cell division.

We then tested the effect of inhibiting GA signalling specifically in the IPR. To do so, we used the *CUP-SHAPED COTYLEDON 2* (*CUC2*) promoter to drive expression of the dominant negative gai-1 protein fused to VENUS (in a *pCUC2::gai-1-VENUS* line). *CUC2* promoter drives expression in a large part of the IPR (including the boundary cells) in the SAM starting from P_4 (Extended Data Fig. 11k). The distribution of cell division angles in the entire SAM or in the IPR of *pCUC2::gai-1-VENUS* plants did not show statistically significant differences with respect to the wild-type (Fig. 6f-i), although unexpectedly, we found in these plants a higher frequency of 80-90° divisions in non-IPR cells. We thus analysed the geometry of *pCUC2::gai-1-VENUS* SAMs and observed that size of the SAM was reduced, whereas it had a significantly higher curvature (Extended Data Fig. 11l-q). This

change in the *pCUC2::gai-1-VENUS* SAM curvature could generate a mechanical stress distribution whereby high circumferential stress starts at a short distance from the SAM centre[42]. This could counteract in part the effect of GA signalling changes by increasing the probability of cell division with circumferential/transverse orientation, thus explaining our observations.

Taken together, these data support a direct role for GA signalling in transverse orientation of the cell division plane in the IPR.

High GA signalling initiates internode specification in the shoot apical meristem (Fig. 7; Extended Data Fig. 13)

Transverse orientation of division planes in the IPR as a result of higher GA signalling activity opens the possibility that GAs pre-organize radial cell files in the epidermis within the SAM to specify the cellular organization later found in the internode epidermis. Indeed, such cell files are often visible in the SAM images of the global *della* mutant (Fig. 6b). Therefore, to further understand the developmental function of the GA signalling spatial pattern in the SAM, we used time-lapse imaging to analyse the cell spatial organization in the IPR in wild type (L*er* and Col-0), global *della* mutant and *pCUC2::gai-1-VENUS* transgenic plants.

We marked L*er* cells above and on the side of P_4 according to their developmental fate (analysed 34 hrs after the first observation, i.e. more than two plastochrones) using three different colours: yellow for those incorporated into the primordia in the vicinity of P_4, green for those located in the IPR and orange for those contributing to both (Fig. 7a-c). At t0 (0 h), 1-2 layers of IPR cells were visible in front of P_4 (Fig. 7a). As expected, when these cells divide, they mostly do it with a transverse division plane (Fig. 7a-c). Similar results were obtained with Col-0 SAMs (focusing on P_3 that had a comparable folding at the boundary than P_4 in L*er*), although in this genotype the formation of the crease at the flower boundary

hides the IPR cells more rapidly (Fig. 7g-i). Thus, their division pattern and localization in the IPR support the idea that these cells correspond to internode precursors.

Compared to L*er*, 1-2 extra layers of IPR cells were observed in front of P_4 at t0 (0 h) in the SAM of global *della* mutants. These cells divided several times in 34 hrs (Fig. 7d-f, compared to 7a-c), and in consequence, the mostly transverse divisions of IPR cells led to a higher population of cells organized in radial cell files (Fig. 7d-f, compared to 7a-c). This indicates that the higher GA signalling activity in global *della* mutant SAMs promotes internode specification. We conducted a similar analysis in *pCUC2::gai-1-VENUS* plants. Since expression of this transgene causes changes in SAM geometry (Extended Data Fig. 11m,n,p,q), we analysed IPR cells above the first primordium showing a comparable folding at the boundary as Col-0 P_3. In these plants, opposite to global *della* mutants, much less cell divisions occurred in the IPR and there was no clear sign of an organization in radial cell files (Fig. 7j-l), thus showing that inhibition of GA signalling in the IPR perturbs the specification of the cellular organisation of internodes in the SAM. In lines with these results, we were able to detect the appearance of internodes in the global *della* mutant just below the SAM using electron microscopy, while flowers remained compacted in L*er* (Fig. 7m-n). By contrast, organs were much more compacted in the SAM of *pCUC2::gai-1-VENUS* than in Col-0 (Fig. 7o-p), consistent with the taller and shorter inflorescence stem of the global *della* mutant[39,43] and *pCUC2::gai-1-VENUS* plants, respectively (Extended Data Fig. 13). Our results thus support the hypothesis that higher GA signalling activity in the IPR specifies the cellular organization of internodes in the SAM, through a regulation of the orientation of cell division planes (Extended Data Fig. 14).

Discussion

408 Here, we developed a new ratiometric GA signalling biosensor, qRGA^{mPFYR}, that provides
409 information on GA function at the cellular level by allowing quantitative mapping of GA
410 signalling activity that results from the combinatorial action of GA and GA receptors
411 concentrations, with minimal interference with the endogenous signalling pathway. To this
412 end, we have engineered a modified DELLA protein, RGA^{mPFYR}, that has lost its capacity to
413 bind DELLA interacting partners but that remains sensitive to GA-induced proteolysis.
414 qRGA^{mPFYR} responds to both exogenous and endogenous changes in GA levels and its
415 dynamic sensing properties allow the assessment of spatio-temporal changes in GA signalling
416 activity during developmental processes. qRGA^{mPFYR} is also a highly flexible tool as it can be
417 adapted to a variety of tissues simply by changing, if needed, the promoter used for its
418 expression and is very likely transferable to other species given the conserved nature of the
419 GA signalling pathway and of the PFYRE motif in angiosperms.
420 Internode development is a key trait for plant architecture and crop improvement. qRGA^{mPFYR}
421 revealed a higher GA signalling activity specifically in cells of the IPR, that are the precursors
422 of internodes. By combining quantitative image analysis and genetics, we show that the GA
423 signalling pattern imposes circumferential/transverse cell division planes in the SAM
424 epidermis, shaping the cell division organization required for internode development. Few
425 developmental regulators of the orientation of the cell division plane during development
426 have been identified[44,45]. Our work provides a striking example of how GAs act in controlling
427 this cellular parameter. Mechanical stress has also been suggested to regulate cell division
428 plane orientation by acting on cortical microtubule[34,41,46] and our results are compatible with a
429 combined effect of mechanical stress and GAs in this regulation. GA signalling could affect
430 the orientation of the cell division plane also through an effect on cortical microtubule
431 orientation[35,36,47]. Likewise, previous works have highlighted the importance of the DELLA
432 interacting proteins TCP14 and 15 in the control of internode patterning[48,49] and these factors

could convey GA action, together with *BREVIPEDICELLUS* (*BP*) and *PENNYWISE* (*PNY*), which regulate internode development and have been shown to affect GA signalling[2,50]. Early cytological studies showed that both the inner tissues and the peripheral zone of the SAM are required for internode development in *Arabidopsis*[2,37]. The fact that GAs positively regulate cell division in the inner tissues supports a dual function of GAs in regulating meristem size and internode at the SAM. Patterns of oriented cell division are also highly regulated in the inner SAM tissues, and this regulation is essential to stem growth[44]. It will be interesting to explore whether GAs also play a role in orienting cell division planes in the inner tissues of the SAM and thus synchronize internode specification and development within the SAM.

Reference

1. Hay, A. & Tsiantis, M. *KNOX* genes: versatile regulators of plant development and diversity. *Development* **137**, 3153–3165 (2010).

2. Smith, H. M. S. & Hake, S. The interaction of two homeobox genes, *BREVIPEDICELLUS* and *PENNYWISE*, regulates internode patterning in the *Arabidopsis* inflorescence. *Plant Cell* **15**, 1717–1727 (2003).

3. Hay, A. *et al.* The Gibberellin pathway mediates KNOTTED1-type homeobox function in plants with different body plans. *Curr. Biol.* **12**, 1557–1565 (2002).

4. Jasinski, S. *et al.* KNOX action in *Arabidopsis* is mediated by coordinate regulation of cytokinin and gibberellin activities. *Curr. Biol.* **15**, 1560–1565 (2005).

5. Shani, E., Yanai, O. & Ori, N. The role of hormones in shoot apical meristem function. *Curr. Opin. Plant Biol.* **9**, 484–489 (2006).

6. Hedden, P. & Sponsel, V. A century of gibberellin research. *J. Plant Growth Regul.* **34**, 740–760 (2015).

7. Davière, J.-M. & Achard, P. Gibberellin signaling in plants. *Development* **140**, 1147–1151 (2013).

8. Silverstone, A. L. *et al.* Repressing a repressor: gibberellin-induced rapid reduction of the RGA protein in *Arabidopsis*. *Plant Cell* **13**, 1555–1566 (2001).

9. Fu, X. *et al.* Gibberellin-mediated proteasome-dependent degradation of the barley DELLA protein SLN1 repressor. *Plant Cell* **14**, 3191–3200 (2002).

10. Ueguchi-Tanaka, M. *et al. GIBBERELLIN INSENSITIVE DWARF1* encodes a soluble receptor for gibberellin. *Nature* **437**, 693–698 (2005).

11. Kinoshita, A. *et al.* Regulation of shoot meristem shape by photoperiodic signaling and phytohormones during floral induction of *Arabidopsis*. *eLife* **9**, e60661 (2020).

12. Serrano-Mislata, A. *et al. DELLA* genes restrict inflorescence meristem function independently of plant height. *Nat. Plants* **3**, 749–754 (2017).

13. Achard, P. *et al.* Gibberellin signaling controls cell proliferation rate in *Arabidopsis*. *Curr. Biol.* **19**, 1188–1193 (2009).

14. Ubeda-Tomás, S. *et al.* Gibberellin signaling in the endodermis controls *Arabidopsis* root meristem size. *Curr. Biol.* **19**, 1194–1199 (2009).

15. Shani, E. *et al.* Gibberellins accumulate in the elongating endodermal cells of *Arabidopsis* root. *Proc. Natl. Acad. Sci.* **110**, 4834–4839 (2013).

16. Tal, I. *et al.* The *Arabidopsis* NPF3 protein is a GA transporter. *Nat. Commun.* **7**, 11486 (2016).

17. Rizza, A., Walia, A., Lanquar, V., Frommer, W. B. & Jones, A. M. *In vivo* gibberellin gradients visualized in rapidly elongating tissues. *Nat. Plants* **3**, 803–813 (2017).

18. Wang, F. *et al.* Biochemical Insights on degradation of *Arabidopsis* DELLA proteins gained from a cell-free assay system. *Plant Cell* **21**, 2378–2390 (2009).

19. Hirano, K. *et al.* Characterization of the molecular mechanism underlying gibberellin perception complex formation in rice. *Plant Cell* **22**, 2680–2696 (2010).

20. Hussain, A., Cao, D. & Peng, J. Identification of conserved tyrosine residues important for gibberellin sensitivity of *Arabidopsis* RGL2 protein. *Planta* **226**, 475–483 (2007).

21. Hussain, A., Cao, D., Cheng, H., Wen, Z. & Peng, J. Identification of the conserved serine/threonine residues important for gibberellin-sensitivity of *Arabidopsis* RGL2 protein. *Plant J.* **44**, 88–99 (2005).

22. Velde, K. V. D., Ruelens, P., Geuten, K., Rohde, A. & Straeten, D. V. D. Exploiting DELLA signaling in cereals. *Trends Plant Sci.* **22**, 880–893 (2017).

23. Shaner, N. C., Steinbach, P. A. & Tsien, R. Y. A guide to choosing fluorescent proteins. *Nat. Methods* **2**, 905–909 (2005).

24. Grefen, C. *et al.* A ubiquitin-10 promoter-based vector set for fluorescent protein tagging facilitates temporal stability and native protein distribution in transient and stable expression studies. *Plant J.* **64**, 355–365 (2010).

25. Weijers, D. *et al.* An *Arabidopsis* minute-like phenotype caused by a semi-dominant mutation in a *RIBOSOMAL PROTEIN S5* gene. *Dev. Camb. Engl.* **128**, 4289–4299 (2001).

26. Tol, N. van *et al.* Enhancement of *Arabidopsis* growth characteristics using genome interrogation with artificial transcription factors. *PLOS ONE* **12**, e0174236 (2017).

27. Wend, S. *et al.* A quantitative ratiometric sensor for time-resolved analysis of auxin dynamics. *Sci. Rep.* **3**, 2052 (2013).

28. Goedhart, J. *et al.* Quantitative co-expression of proteins at the single cell level – application to a multimeric FRET sensor. *PLOS ONE* **6**, e27321 (2011).

29. Achard, P. *et al.* DELLAs contribute to plant photomorphogenesis. *Plant Physiol.* **143**, 1163–1172 (2007).

30. Gendreau, E. *et al.* Cellular basis of hypocotyl growth in *Arabidopsis thaliana. Plant Physiol.* **114**, 295–305 (1997).

31. Savaldi-Goldstein, S., Peto, C. & Chory, J. The epidermis both drives and restricts plant shoot growth. *Nature* **446**, 199–202 (2007).

32. Galvan-Ampudia, C. S. *et al.* Temporal integration of auxin information for the regulation of patterning. *eLife* **9**, e55832 (2020).

33. Uyttewaal, M. *et al.* Mechanical stress acts via katanin to amplify differences in growth rate between adjacent cells in *Arabidopsis. Cell* **149**, 439–451 (2012).

34. Burian, A. *et al.* A correlative microscopy approach relates microtubule behaviour, local organ geometry, and cell growth at the *Arabidopsis* shoot apical meristem. *J. Exp. Bot.* **64**, 5753–5767 (2013).

35. Marc, J. & Hackett, W. P. Changes in the pattern of cell arrangement at the surface of the shoot apical meristem in *Hedera helix* L. following gibberellin treatment. *Planta* **186**, 503–510 (1992).

36. Locascio, A., Blázquez, M. A. & Alabadí, D. Dynamic regulation of cortical microtubule organization through prefoldin-DELLA interaction. *Curr. Biol.* **23**, 804–809 (2013).

37. Vaughan, J. G. The morphology and growth of the vegetative and reproductive apices of *Arabidopsis thaliana* (L.) Heynh., *Capsella bursa-pastoris* (L.) Medic. and *Anagallis arvensis* L. *J. Linn. Soc. Lond. Bot.* **55**, 279–301 (1955).

38. Jackson, D., Veit, B. & Hake, S. Expression of maize *KNOTTED1* related homeobox genes in the shoot apical meristem predicts patterns of morphogenesis in the vegetative shoot. *Development* **120**, 405–413 (1994).

39. Cheng, H. *et al.* Gibberellin regulates *Arabidopsis* floral development via suppression of DELLA protein function. *Development* **131**, 1055–1064 (2004).

40. Gallego-Giraldo, C. *et al.* Role of the gibberellin receptors GID1 during fruit-set in *Arabidopsis*. *Plant J.* **79**, 1020–1032 (2014).

41. Louveaux, M., Julien, J.-D., Mirabet, V., Boudaoud, A. & Hamant, O. Cell division plane orientation based on tensile stress in *Arabidopsis thaliana. Proc. Natl. Acad. Sci.* **113**, E4294–E4303 (2016).

42. Hamant, O. *et al.* Developmental patterning by mechanical signals in *Arabidopsis. Science* **322**, 1650–1655 (2008).

43. Kumar, S. V. *et al.* Transcription factor PIF4 controls the thermosensory activation of flowering. *Nature* **484**, 242–245 (2012).

44. Bencivenga, S., Serrano-Mislata, A., Bush, M., Fox, S. & Sablowski, R. Control of oriented tissue growth through repression of organ boundary genes promotes stem morphogenesis. *Dev. Cell* **39**, 198–208 (2016).

45. Yoshida, S. *et al.* Genetic control of plant development by overriding a geometric division rule. *Dev. Cell* **29**, 75–87 (2014).

46. Rasmussen, C. G. & Bellinger, M. An overview of plant division-plane orientation. *New Phytol.* **219**, 505–512 (2018).

47. Wenzel, C. L., Williamson, R. E. & Wasteneys, G. O. Gibberellin-induced changes in growth anisotropy precede gibberellin-dependent changes in cortical microtubule orientation in developing epidermal cells of barley leaves. kinematic and cytological studies on a gibberellin-responsive dwarf mutant, M489. *Plant Physiol.* **124**, 813–822 (2000).

48. Davière, J.-M. *et al.* Class I TCP-DELLA interactions in inflorescence shoot apex determine plant heigh. *Curr. Biol.* **24**, 1923–1928 (2014).

49. Kieffer, M., Master, V., Waites, R. & Davies, B. TCP14 and TCP15 affect internode length and leaf shape in *Arabidopsis. Plant J.* **68**, 147–158 (2011).

50. Khan, M. *et al.* Repression of lateral organ boundary genes by *PENNYWISE* and *POUND-FOOLISH* is essential for meristem maintenance and flowering in *Arabidopsis*. *Plant Physiol.* **169**, 2166–2186 (2015).

51. Koini, M. A. *et al.* High temperature-mediated adaptations in plant architecture require the bHLH transcription factor PIF4. *Curr. Biol.* **19**, 408–413 (2009).

52. Lee, S. *et al.* Gibberellin regulates *Arabidopsis* seed germination via *RGL2*, a *GAI*/*RGA*-like gene whose expression is up-regulated following imbibition. *Genes Dev.* **16**, 646–658 (2002).

53. Pfeiffer, A. *et al.* Integration of light and metabolic signals for stem cell activation at the shoot apical meristem. *eLife* **5**, e17023 (2016).

54. Karimi, M., Inzé, D. & Depicker, A. GATEWAY^{TM} vectors for Agrobacterium-mediated plant transformation. *Trends Plant Sci.* **7**, 193–195 (2002).

55. Galinha, C. *et al.* PLETHORA proteins as dose-dependent master regulators of Arabidopsis root development. *Nature* **449**, 1053–1057 (2007).

56. Simon, M. L. A. *et al.* A PtdIns(4)P-driven electrostatic field controls cell membrane identity and signalling in plants. *Nat. Plants* **2**, 1–10 (2016).

57. Shcherbakova, D. M., Hink, M. A., Joosen, L., Gadella, T. W. J. & Verkhusha, V. V. An orange fluorescent protein with a large stokes shift for single-excitation multicolor FCCS and FRET imaging. *J. Am. Chem. Soc.* **134**, 7913–7923 (2012).

58. Resentini, F. *et al.* TCP14 and TCP15 mediate the promotion of seed germination by gibberellins in *Arabidopsis thaliana*. *Mol. Plant* **8**, 482–485 (2015).

59. Gallego-Bartolomé, J. *et al.* Molecular mechanism for the interaction between gibberellin and brassinosteroid signaling pathways in *Arabidopsis*. *Proc. Natl. Acad. Sci.* **109**, 13446–13451 (2012).

60. de Lucas, M. *et al.* A molecular framework for light and gibberellin control of cell elongation. *Nature* **451**, 480–484 (2008).

61. Castrillo, G. *et al.* Speeding cis-trans regulation discovery by phylogenomic analyses coupled with screenings of an arrayed library of *Arabidopsis* transcription factors. *PLOS ONE* **6**, e21524 (2011).

62. Vernoux, T., Kronenberger, J., Grandjean, O., Laufs, P. & Traas, J. PIN-FORMED 1 regulates cell fate at the periphery of the shoot apical meristem. *Dev. Camb. Engl.* **127**, 5157–5165 (2000).

63. Rozier, F., Mirabet, V., Vernoux, T. & Das, P. Analysis of 3D gene expression patterns in plants using whole-mount RNA in situ hybridization. *Nat. Protoc.* **9**, 2464–2475 (2014).

64. Schroeder, W., Martin, K. & Lorensen, B. *The visualization toolkit: an object-oriented approach to 3D graphics*. (Kitware, 2006).

65. Landrein, B. *et al.* Mechanical stress contributes to the expression of the *STM* homeobox gene in *Arabidopsis* shoot meristems. *eLife* **4**, e07811 (2015).

Methods

Growth conditions and Plant material

Plants were grown on soil or *in vitro* on 1x Murashige-Skoog (MS) medium (Duchefa) supplemented with 1% sucrose and 1% agar (Sigma) under standard conditions (16h photoperiod at 22°C), except for hypocotyl and root growth experiments, for which the seedlings were grown on vertical plates under continuous light and 22°C.

We used the following *Arabidopsis* mutants and transgenic lines in the L*er* background: *gai-t6 rga-t2 rgl1-1 rgl2-1* quadruple *della*[39], *gai-t6 rga-t2 rgl1-1 rgl2-1 rgl3-4* global *della*[51] or Col-0: *pGID1a::GID1a-GUS*, *pGID1b::GID1b-GUS*, *pGID1c::GID1c-GUS*, *pGAI::GUS*, *pRGA::GUS*, *pRGL1::GUS*, *rgl2-5* (a promoter trap GUS line)[52], *pRGA::GFP-RGA*[8], *pRGL3::RGL3-GFP*, *pCLV3::mCherry-NLS*[53], *nlsGPS1*[17].

All other transgenic lines were generated in the Col-0 background. To generate these lines and to perform transient assays in *Nicotiana benthamiana* leaves, plasmids were constructed in the following way. RGA cDNA (Agi code AT2G01570) and RGA^{m1}, $RGA^{m2,}$ RGA^{m3} and RGA^{m4} mutant variants were obtained by PCR using specific primers numbered 1 to 8 in Supplementary Table 1, and inserted into pDONR221 (Thermo Fisher Scientific) by Gateway cloning and recombined with pB7FWG2[54] to generate *p35S::RGA-GFP* and *p35S::*$RGA^{m1/m2/m3/m4}$*-GFP*. To generate *pRPS5a::qRGA*^{mPFYR}, *pUBQ10:qRGA*^{mPFYR}, *pRPS5a::*$RGA^{m1/m3/m4}$*-VENUS-2A-BFP*, *pUBQ10::*$RGA^{m1/m3/m4}$*-VENUS-2A-BFP* and *pCUC2::gai-1-VENUS*, the promoter region of *pRPS5a* (1.7 kb fragment), *pUBQ10* (2.5 kb fragment) or *pCUC2* (3.2 kb fragment) inserted into pDONR P4-P1R (Thermo Fisher Scientific), *RGA*^{mPFYR} *-VENUS*, *RGA*$^{m1/m3/m4}$ *-VENUS* or *gai-1* cDNA inserted into pDONR221, and *2A-TagBFP* or *VENUS* (for *pCUC2::gai-1-VENUS)* inserted into pDONR P2R-P3 (Thermo Fisher Scientific), were recombined into pB7m34GW[54]. To obtain *pUBQ10::GID1a-mCherry*, *GID1a* cDNA inserted into pDONR221 was recombined with

pDONR P4-P1R-*pUBQ10* and pDONR P2R-P3-*mCherry* into pB7m34GW. *p35S:IDD2-RFP* was obtained by recombining *IDD2* cDNA inserted in pDONR221 into pB7RWG2[54]. To get *pGID1b::2xmTQ2-GID1b*, a 3.9-kb fragment upstream of the coding region of *GID1b* and a 4.7-kb fragment including *GID1b* cDNA (1.3 kb) and terminator (3.4 kb) were first amplified using primers in Supplementary Table 1, then inserted into pDONR P4-P1R (Thermo Fisher Scientific) and pDONR P2R-P3 (Thermo Fisher Scientific), respectively, and finally recombined into pGreen 0125[55] destination vector with pDONR221 2xmTQ2[56] by Gateway cloning. To make *pCUC2::LSSmOrange*, the promoter sequence of *CUC2* (3229 bp upstream the ATG), followed by the coding sequence for the large stokes shift mOrange (LSSmOrange)[57] with a N7 nuclear localization signal, and the NOS transcription terminator, was assembled into the pGreen Kanamycin destination vector using 3 fragment Gateway recombination system (Invitrogen). For transactivation assays, *pTCP-LUC* and *pBRE-LUC* reporter constructs (containing synthetic promoters) and *p35S::3xHA-VP16-TCP14* and *p35S::3xHA-VP16-BZR1* encoding effector proteins were used as previously described[58,59] . Plant binary vectors were inserted into *Agrobacterium tumefaciens* GV3101 strain and respectively introduced into *Nicotiana benthamiana* leaves by agro-infiltration and *Arabidopsis* Col-0 by floral dip. *pUBQ10::qRGA*^{mPFYR} *pUBQ10::GID1a-mCherry* and *pCLV3::mCherry-NLS qRGA*^{mPFYR} were isolated from F3 and F1 progeny of the appropriate crosses, respectively.

Pharmacological treatments

Chemical treatments with GA (GA_3, Sigma or Duchefa) and paclobutrazol (PAC, Duchefa) were performed at the concentrations and time indicated in figures. For Y2H assays, 100 µM GA_3 were added in selective media to promote interaction between RGA and GID1. For RGA and RGA$^{m1/m2/m3/m4}$ degradation kinetics, *N. benthamiana* agro-infiltrated leaf discs were

642 incubated with 100 µM GA_3 and 100 mM cycloheximide (Sigma) over 300 min. For
643 hypocotyl length measurements and fluorescence analyses of $qRGA^{mPFYR}$ hypocotyls and
644 roots, seedlings were grown for 5 days on MS agar medium and then transferred for 4 days on
645 MS agar plates supplemented with 5 µM PAC or 10 µM GA_3. For GA_3 treatment on
646 $qRGA^{mPFYR}$, GA_{4+7} treatment on nlsGPS1, and GA-Fl treatment on L*er*, dissected shoot
647 apices were inserted into Apex Culture Medium (ACM, 1/2x MS medium (Duchefa), 1%
648 sucrose, 1% agarose, 2 mM MES (Sigma), 1x vitamin solution (myo-Inositol 100 mg/L,
649 nicotinic acid 1 mg/L, pyridoxine hydrochloride 1 mg/L, thiamine hydrochloride 10 mg/L,
650 glycine 2 mg/L), 200 nM N6-Benzyladenine) with indicated concentrations of GA/GA-Fl,
651 and also immersed under 200 µl of GA/GA-Fl solution of indicated concentrations for a
652 indicated period of time. For PAC treatment on $qRGA^{mPFYR}$, 50 µM PAC were sprayed on the
653 whole inflorescence every two days for a period of 5 days before observation.
654

655 **Yeast two-hybrid assays**

656 For Y2H assays, both the full-length and the C-terminal part of RGA and $RGA^{m1/m2/m3/m4}$
657 (named M5 version, amino acids 199 to 587; the N-terminal part is subject to self-activation
658 in yeast[60]) inserted into pDONR221 were recombined into pGBKT7 (Clontech) to obtain BD-
659 RGA, BD-$RGA^{m1/m2/m3/m4}$, BD-M5RGA and BD-$M5RGA^{m1/m2/m3/m4}$. On the other hand, JAZ1,
660 TCP14, IDD2, BZR1, GID1a, GID1b and GID1c cDNAs inserted into pDONR221 were
661 fused to the activation domain GAL4 (AD) after recombination into pGADT7 (Clontech).
662 Direct interaction assays were carried out following the Clontech procedures. Briefly, BD-
663 M5DELLA and AD-JAZ1, AD-TCP14, AD-IDD2, AD-BZR1 and, on the other hand, BD-
664 DELLA (full length) and AD-GID1 constructs were co-transformed in the yeast strain AH109
665 and interactions tests were surveyed on selective medium lacking tryptophan, leucine and

histidine. In some cases, the medium was supplemented with 3-amino-1, 2, 4 triazole (3AT, Sigma) or with GA to promote interaction between DELLA and GID1.

To confirm that the RGA^{m2} mutation impaired interaction with all RGA protein partners, we used the C-terminal part of RGA and RGA^{m2} (amino acids 199 to 587) and of GAI (amino acids 148 to 533) for positive control, to probe the Arabidopsis transcription factors REGIA + REGULATORS (RR) arrayed library, following the protocol described in Castrillo G. et al.[61]. TFs in the RR library were fused to GAL4 activation domain of the pDEST22 vector and independently transformed into the yeast strain YM4271 in 96-well plates. The RGA^{m2} protein fused to the GAL4 BD in the pDEST32 vector was transformed into the pJ694 yeast strain and used as bait. Replicates of the library were grown overnight on SD-Trp solid media and inoculated together with 100 µL of an overnight RGA^{m2} culture grown on SD-Leu on microtiter plates containing 100 µL of YPDA per well. Plates were incubated for 2 days at 30°C for mating, and diploid colonies were selected in new 96-well plates containing 200 µL of SD-Leu/Trp. 5 µL of the diploid cell cultures were lastly tested for protein interaction by placing them on solid SD medium lacking both Leu and Trp (positive growth control), and on SD medium lacking Leu, Trp and His, in the presence of different concentrations of 3-aminotriazol (3-AT) (Sigma-Aldrich). Results were expressed in the form of a heat map for the strength of interaction according to the colony growth after five days of incubation at 30°C.

Co-immunoprecipitation assays

CoIP assays of IDD2-RFP with RGA-GFP or RGA^{m2}-GFP were performed on *N. benthamiana* agro-infiltrated leaves with *p35S::IDD2-RFP*, *p35S::RGA-GFP* or *p35S::RGA^{m2}-GFP*. Three days after infiltration, total proteins were extracted with the native extraction buffer [Tris-HCl (pH 7.5) 50 mM, glycerol 10%, Nonidet P-40 0.1% supplemented

with Complete Protease Inhibitors 1X (Roche)], and then incubated for 2h at 4°C with 50 µl of anti-GFP antibody conjugated with paramagnetic beads (Miltenyi Biotec). After incubation, samples were loaded onto a magnetic column system (µ columns ; Miltenyi Biotec) to recover the immunoprotein complexes according to manufacturer's protocol. The immunoprecipitated (RGA-GFP and RGA^{m2}-GFP) and co-immunoprecipitated (IDD2-RFP) proteins were detected by western-blot with anti-GFP (JL8; Clontech) and anti-RFP (6G6; Chromotek), respectively.

Immunodetection analyses

Plant materials were ground in 2x SDS-PAGE buffer followed by heating at 95°C for 5 min. After centrifugation at 13000 *g* for 5 min, total proteins were separated on 8.5% SDS-PAGE gel and transferred to an immobilon-P (PVDF) membrane (Millipore). Membranes are then saturated with blocking buffer (TBS 1x, Tween-20 0.1%; milk 5%) and incubated with a 2000-fold dilution of anti-GFP (JL8; Clontech), anti-RGA (6G6; Chromotek), anti-HA (Sigma) or anti-actin (Agrisera) antibodies, and a 5000-fold dilution of peroxidase-conjugated goat anti-rabbit or mouse IgG (Invitrogen). Signals were detected using the Luminata Forte Western HRP Substrate (Millipore).

Transactivation assays

Transactivation assays were performed using the Dual-Glo Luciferase Assay System (Promega) according to manufacturer's instructions. Briefly, *N. benthamiana* leaves were agro-infiltrated with *pTCP-LUC* and *pBRE-LUC* reporter constructs, *p35S::3xHA-VP16-TCP14* or *p35S::3xHA-VP16-BZR1* encoding effector proteins, and *p35S::RGA-GFP* or *p35S::RGA^{m2}-GFP*. Three days after infiltration, total proteins were extracted in lysis buffer (Promega), then Firefly and control Renilla LUC activities were quantified with FLUOstar

Omega luminometer (BMG Labtech) using OMEGA2 software version 5.50 R4. For loading control, protein levels were analysed by immunodetection.

GUS staining

For GUS expression detection in inflorescence apex, 28-d-old plants grown under LD conditions were used. After fixation in 90% cold acetone at room temperature for 20 min, shoot apexes were transferred into GUS staining solution containing 1 mM potassium ferrocyanide, 1 mM potassium ferricyanide and 1 mg/ml 5-bromo-4-chloro-3-indolyl-*ß*-D-glucuronide (X-Gluc), vacuum-infiltrated on ice for 15 min, and incubated overnight at 37 °C in dark before washing with ethanol series and microscope detection. For the experiment with seedlings, 7-d-old plantlets grown in vitro under LD conditions were vacuum-infiltrated for 15 min in GUS staining solution containing 2 mM potassium ferrocyanide, 2 mM potassium ferricyanide and 0.25 mg/ml X-Gluc, and incubated at 37°C for 24 h. Then GUS solution was replaced with ethanol 70% and seedlings were observed using optical microscope.

***In situ* hybridizations**

RNA in situ hybridizations were performed according to Vernoux et al.[62] with some minor modifications on fixation. Briefly, shoot apices with ~1cm stem were collected and immediately fixed in FAA solution (3.7% Formaldehyde, 5% Acetic Acid, 50% Ethanol) precooled at 4 ºC. After vacuum treatments for 2x 15 min, the fixative was changed and the samples were incubated overnight. Antisense probes of the cDNA and 3'-UTR of *GID1a*, *GID1b*, *GID1c*, *GAI*, *RGL1*, *RGL2* and *RGL3* were synthesized as described in Rozier et al.[63] using primers indicated in Supplementary Table 1. Immunodetection of the digoxigenin-labelled probes was performed using an anti-digoxigenin antibody, and sections were stained with 5-Bromo-4-chloro-3-indoryl Phosphate (BCIP)/Nitroblue Tetrazolium (NBT) solutions.

Microscopy

For confocal microscopy observations of hypocotyl, complete seedlings were put on slides and images were obtained with a Zeiss LSM 780 confocal microscope. SAM live imaging was performed as described[32]. Briefly, dissected SAMs were let to recover overnight after dissection. Confocal images were taken with a Zeiss LSM 710 or 700 confocal laser scanning microscope equipped with a water-dipping lens (W Plan-Apochromat 40x/1.0 DIC). The confocal settings were as previously described[32] and detailed below. To observe GFP or GFP with propidium iodide (PI), a laser of 488 nm was used to excite, and the emission for GFP was 500-520 nm (in some cases it was 500-540 nm), for PI was 610-650 nm. For imaging of $qRGA^{mPFYR}$ or $qRGA^{mPFYR}$ with mCherry and PI, lasers of 514 nm, 405 nm, 561 nm and 488 nm were used for the excitation of VENUS, TagBFP, mCherry and PI, respectively, and the corresponding emission wavelength was 520-560 nm, 430-460 nm, 580-615 nm and 620-660 nm. mTURQUOISE2 (mTQ2) was excited by 445 nm laser and the emission range was 470-510 nm. For FRET detection of nlsGPS1, an acquisition mode of spectral imaging (λ-scan) with emission wavelength from 461 nm to 597 nm was used with excitation at 458 nm.

For optical microscopy, photographs of plants were taken with a LEICA MZ12 stereoscopic microscope equipped with a ZEISS AxioCam ICc5 camera head or Canon camera.

For scanning electronic microscopy of fresh shoot apex, a Hirox SH-3000 table-top microscope equipped with Coolstage (-20 °C to -30 °C) was used.

Image processing

Confocal stacks were processed in Fiji (fiji.sc) to get max projection or orthogonal views. Older primordia were also removed in Fiji. For 3D visualization of confocal stacks, we used

the Zeiss ZEN2 software (Fig. 7) and a rendering using the VTK library[64] (Fig. 5e, Fig. 6). In both cases, parameters were adjusted accordingly to show mainly the L1 cells.

Quantification and statistical analysis

GA sensor quantification

For qRGA^{mPFYR} quantification and visualization, images of hypocotyls were analyzed using a Python script that performs nuclei detection and signal quantification in 3D. The details of the algorithms used in the analysis are provided in Supplementary Method 1 (Section 2 – Nuclei detection and signal quantification).

For nlsGPS1 quantification and visualization, a series of Fiji macros were used (macros are deposited in Protocol Exchange). Briefly, the "seg-auto.ijm" macro was run for segmentation of nuclei based on the sum of signals from all the 14 channels of the spectral imaging. After removing little objects corresponding to signal noise using the "object-screening.ijm" macro, the ratio of DxAm (channel 8) to DxDm (channel 3) of each segmented nucleus was calculated by running the "3D-ratio.ijm", and from here, the 3D construction of the SAM, with every nucleus showing its ratio value, was also achieved and printed. Statistical analysis was done in R.

SAM image sequence analysis

To analyze time-lapse confocal acquisitions of SAMs and obtain quantitative measures of GA signalling as well as cellular growth parameters, we developed a computational pipeline. It consists of 3D watershed segmentation for cell identification from the PI staining, nuclei detection and qRGA quantification, temporal registration using the PI image channel and surfacic growth estimation based on expert cell lineages. Individual SAM sequences were then aligned in order to perform population-scale statistics. Extensive details on the algorithms used in this pipeline are provided in Supplementary Method 1.

Hypocotyl length measurement

To measure hypocotyl length, seedlings were grown in vertical MS medium (Duchefa) with 0.8% (w/v) phytoagar and 1% sucrose for 5 days and transferred to MS, MS supplemented with 10 µM GA3 or 5 µM Paclobutrazol for 4 days in continuous light at 22ºC. Plates were scanned and hypocotyl length was measured from the images using Fiji.

Cell division orientation quantification

New cell walls were identified by comparing images obtained at 0 h and 10 h, and masked with a manually drawn line in Fiji. Then, a macro was used to skeletonize and then to measure the angles of the drawn cell walls with an expert-defined centre of the SAM. Further angle frequency distribution was done in Excel using Pivot table. Statistical analysis of Kolmogorov-Smirnov test was performed using an online tool: http://www.physics.csbsju.edu/stats/KS-test.n.plot_form.html.

Curvature quantification

The MorphoGraphX software was used to quantify cellular curvature of L1 cells of SAMs of different genetic backgrounds. Statistical analysis was done in R.

Meristem size measurement

To measure meristem size, a method described before was used[65]. Briefly, the SAM radius was determined by drawing a circle that covers I_1 and I_2 and that the center of which is roughly overlapping with the geometrical center of the SAM surface using Fiji software. Statistical analysis was done in R.

Synthesis and characterization of GA-Fluorescein (GA-Fl)

GA-Fluorescein (GA-Fl) were synthesized using a previously described protocol[15]. Extensive details on synthesis and characterization are provided in Supplementary Method 2.

Figure legends

Figure 1. The modified RGA^{m2} protein is an inactive DELLA that remains sensitive to GA.

a, Schematic representation of the domain structure of a typical DELLA protein. The nucleic acids and amino acids mutated in RGA^{m2} are indicated in red. **b**, Yeast two hybrid (Y2H) assays in which RGA and RGA^{m2} were tested pairwise with four known DELLA-interacting partners: JAZ1, TCP14, IDD2 and BZR1. Empty pGBKT7 and pGADT7 vectors were included as negative controls. Photos show the growth of the yeast on control media (GM) and on selective media (SM). **c**, Pairwise Y2H interaction assays between RGA or RGA^{m2} and the three GA receptors GID1a, GID1b and GID1c. Photos show the growth of the yeast on control media (GM), selective media (SM) and SM media supplemented with 100 µM GA_3. **d**, Time-course analysis of GA-induced degradation of RGA (upper panel) and RGA^{m2} protein (lower panel). Immunodetection of RGA-GFP and RGA^{m2}-GFP protein in *35S::RGA-GFP* and *35S::RGA^{m2}-GFP N. benthamiana* agro-infiltrated leaves treated with 100 mM cycloheximide (CHX) and 100 µM GA_3 for the indicated times. Numbers indicate RGA-GFP and RGA^{m2}-GFP levels relative to Actin levels, used as loading control. **e**, Coimmunoprecipitation assays between RGA or RGA^{m2} and IDD2. Protein extracts from different combinations of *N. benthamiana* agro-infiltrated leaves with *35S::RGA-GFP*, *35S::RGA^{m2}-GFP* and *35S::IDD2-RFP* were immunoprecipitated with anti-GFP antibodies. The co-immunoprecipitated protein (IDD2-RFP) was detected by anti-RFP antibodies. **f-g,** Effect of RGA and RGA^{m2} on BZR1 (**f**) and TCP14 (**g**) transcriptional activities in *N. benthamiana* agro-infiltrated leaves with a combinations of BZR1, TCP14, RGA and RGA^{m2} effector constructs and corresponding Luciferase/Renilla reporter constructs, as indicated (top panels). Transcriptional activities are represented as the ratio of Luciferase and Renilla (used as internal control) activities, relative to the value obtained for the reporter construct alone

that was set to 1. Different letters denote significant differences ($p < 0.05$) using ANOVA Tukey's tests for multiple comparisons. Bottom panels: immunodetection of RGA-GFP, RGA^{m2}-GFP, HA-VP16-BZR1 and HA-VP16-TCP14 from *N. benthamiana* agro-infiltrated leaves used for transcriptional activity assays.

Extended Data Figure 1. Characterization of mutant DELLA proteins.

a, Position of the mutated nucleic acids and amino acids of the four candidate modified DELLA proteins used in the study: RGA^{m1}, RGA^{m2}, RGA^{m3}, RGA^{m4}. *: stop codon. **b**, Pairwise Y2H interaction assays between RGA, RGA^{m1}, RGA^{m3}, RGA^{m4} and three DELLA-interacting proteins, JAZ1, TCP14 and IDD2. Empty pGBKT7 and pGADT7 vectors were included as negative controls. Photos show the growth of the yeast on control media (GM) and on selective media (SM). **c**, Pairwise Y2H interaction assays between RGA, RGA^{m3}, RGA^{m4} and GID1a, GID1b and GID1c. Photos show the growth of the yeast on control media (GM), selective media (SM) and SM media supplemented with 100 µM GA_3. **d**, Time-course analysis of GA-induced degradation of RGA, RGA^{m2}, RGA^{m3} and RGA^{m4}. Left panel: Immunodetection of RGA-GFP, RGA^{m2}-GFP, RGA^{m3}-GFP and RGA^{m4}-GFP proteins respectively in *35S::RGA-GFP*, *35S::RGA^{m2}-GFP*, *35S::RGA^{m3}-GFP* and *35S::RGA^{m4}-GFP* *N. benthamiana* agro-infiltrated leaves treated with 100 mM cycloheximide (CHX) and 100 µM GA_3 for the indicated times. Actin is used as sample loading control. Right panel: Quantification of the immunoblot signals depicted as a graph. Values indicate RGA-GFP, RGA^{m2}-GFP, RGA^{m3}-GFP and RGA^{m4}-GFP signals relative to Actin signals.

Extended Data Figure 2. RGA^{m2} loses its ability to bind with RGA-interacting partners.

Extended pairwise Y2H interaction assays between GAI, RGA and RGA^{m2} and with 91 DELLA-interacting transcription factors. The colour code and numbers (0 to 5) indicate the

strength of the interactions based on the size of the yeast colonies on selective media (without leucine, tryptophan and adenine: -LWH). Empty pGBKT7 and pGADT7 vectors were included as negative controls.

Figure 2. The qRGA^{mPFYR} sensors monitors changes in GA levels.

a, Schematic representation of the qRGA^{mPFYR} construct composed of two elements: the sensor module (RGA^{mPFYR}-VENUS), and the normalization element (TagBFP fused with a nuclear localization signal (NLS)). The two elements are linked by a 2A self-cleaving peptide, and driven by the same promoter allowing stoichiometric expression. GA signalling activity is measured as 3 minus the ratio between VENUS and TagBFP signal intensities. **b**, TagBFP expression pattern of *pUBQ10::qRGA^{mPFYR}* and *pRPS5a::qRGA^{mPFYR}* sensors monitored in cotyledon, vegetative SAM, hypocotyl and root of 7-day-old seedlings. **c**, Hypocotyl length of wild-type (Col-0) and *pUBQ10::qRGA^{mPFYR}* seedlings. Upper panel: Hypocotyl length at 5 and 9 days after sowing (DAS). Lower panel: Hypocotyl length of 9-d-old seedlings grown for 4 days on MS media and then transferred to MS media supplemented with 5 µM PAC or 10 µM GA_3, and controls (Mock). Different letters denote significant differences ($p < 0.05$) using ANOVA Tukey's tests for multiple comparisons. **d**, Boxplot representations of the number of rosette leaves (upper panel) and final plant height (lower panel) of wild-type (Col-0) and *pRPS5a::qRGA^{mPFYR}* adult plants. *P* values are from Wilcoxon rank-sum tests. **e**, Representative confocal images of RGA^{mPFYR}-VENUS and TagBFP signals in hypocotyls of 9-d-old *pUBQ10::qRGA^{mPFYR}* seedlings that have been treated with PAC or GA (and Mock control), as in **c**. The *pRGA::GFP-RGA* transgenic line was used as a positive control of the treatments. Intensity heatmap representation of GA signalling activity is shown with the same colour code in the last vertical panel. **f**, Boxplot representation of GA signalling activity (means of at least 8 seedlings) measured in seedling hypocotyls grown in the same conditions

as in **c** and shown in **e**. For statistical analysis, a Kruskal-Wallis test between MS/PAC and MS/GA conditions was applied. The experiment was repeated twice with similar results. **g**, Hypocotyl length measurement of wild-type (Col-0) and *pUBQ10::qRGA^{mPFYR}* seedling hypocotyls grown either in dark or light conditions from day 2 to day 9 post sowing. **h**, Boxplot representation of GA signalling activity measured in basal region of seedling hypocotyls (means of 15 to 31 seedlings) grown in light or dark conditions, at 3, 5 and 7 DAS. A Kruskal-Wallis test between light and dark-grown seedlings was applied. The experiment was repeated twice with similar results.

Extended data Figure 3. Expression patterns of *pUBQ10::qRGA^{mPFYR}* and *pRPS5a::qRGA^{mPFYR}* in the SAM and responses of *pRPS5a::qRGA^{mPFYR}* to changes in GA levels.

a-c, Fluorescence signals of RGA^{mPFYR}-VENUS (a), TagBFP-NLS (b) and merge channels (c) in *pUBQ10::qRGA^{mPFYR}* inflorescence SAM. **d-f**, Fluorescence signals of RGA^{mFPYR}-VENUS (d), TagBFP-NLS (e) and overlay (f) in *pRPS5a::qRGA^{mPFYR}* SAM. **g**, Representative growing wild-type (Col-0) and *pRPS5a::qRGA^{mPFYR}* plants with flowers and elongated siliques indicative of normal fertility (arrows). **h-p**, Fluorescence signals of RGA^{mPFYR}-VENUS (h, m), TagBFP-NLS (i, n) and overlay (j, o) in *pRPS5a::qRGA^{mPFYR}* SAM, 2h after a treatment with 100 µM GA_3 (h-j) and mock controls (m-o). (k, p) Heatmap representations of GA signalling activity from (j, o). The older floral primordia were removed digitally. (l) Boxplot representation of GA signalling activity in SAM treated as in (j, o). **q-u**, Fluorescence signals of RGA^{mFPYR}-VENUS (q, v), TagBFP-NLS (r, w) and overlay (s, x) in *pRPS5a::qRGA^{mPFYR}* SAM, 5 days after a treatment with 50 µM PAC (v-x) and mock (q-s). (t, y) Heatmap representations of GA signalling activities from (s, x). Older floral primordia were removed digitally. (u) Boxplot representation of GA signalling activity is SAM treated

as in (s, x). *P* values are from Wilcoxon rank-sum tests. Experiments were repeated twice with similar results. Scale bars = 20 μm (a-f, h-j, m-o, q-s, v-x) and 1 mm (g).

Extended Data Figure 4. Behaviour of the different GA signalling sensor lines in response to changes in GA levels in seedling root.

Representative VENUS and TagBFP signals obtained in seedling roots of qRGA^{mPFYR}, qRGA^{m3} and qRGA^{m4} lines driven with *pUBQ10* and *pRPS5a* promoters, treated with 5 μM PAC or 10 μM GA_3 (and Mock controls), as in Figure 2. *pRGA::GFP-RGA* is used as a positive control of GA and PAC treatments.

Extended data Figure 5. Dose and temporal responses of qRGA^{mPFYR} to exogenous GA treatment in the SAM.

a-i, Overlay of VENUS and TagBFP maximum intensity projection (a-d) and corresponding heatmap representation of GA signalling activity (e-h) of qRGA^{mPFYR} SAMs treated for 3 h with 1 μM (b, f), 10 μM (c, g) and 100 μM (d, h) GA_3, and Mock controls (a, e). Boxplot representation of GA signalling activity is shown in (i). **j-z**, Overlay of VENUS and TagBFP maximum intensity projection (j-m, r-u) and corresponding heatmap representation of GA signalling activity (n-q, v-y) of qRGA^{mPFYR} SAM treated with 100 μM GA_3 for 1 h (s, w), 2 h (t, x) and 3 h (u, y), and mock controls (j-q). Boxplot representation of GA signalling activity is shown in (z). *P* values are from Wilcoxon rank-sum tests. Experiments were repeated twice with similar results. Scale bars = 20 μm.

Figure 3. The qRGA^{mPFYR} sensor signal depends on GA receptor activity.

a-c, Expression pattern of *GID1a*, *GID1b* and *GID1c* in shoots (upper panel) and root tips (lower panel) of 7-d-old *pGID1a::GID1a-GUS* (a), *pGID1b::GID1b-GUS* (b) and *pGID1c::*

GID1c-GUS (c) seedlings. **d**, Boxplot representation of GA signalling activity in hypocotyls of 5-d-old *pUBQ10::RGA*^{mPFYR} (pink) and *pUBQ10::RGA*^{mPFYR} *pUBQ10::GID1a-mCherry* (cyan) seedlings treated with 100 μM GA_3 for 30, 90 and 180 min, and untreated controls. *P*-values are from Kruskal-Wallis tests.

Extended data Figure 6. Expression patterns of GA receptors in the SAM.

a-c, Expression patterns of *GID1a*, *GID1b* and *GID1c* in the SAM of *pGID1a::GID1a-GUS* (a), *pGID1b::GID1b-GUS* (b) and *pGID1c::GID1c-GUS* (c) adult plants. **d-l**, *In situ* localization of *GID1a* (d-f), *GID1b* (g-i) and *GID1c* (j-l) mRNA in inflorescence apex. 3 consecutive sections are shown for each. **m**, Maximum intensity projection showing the expression of *pGID1b::2xmTQ2-GID1b*. Scale bars = 200 μm (a-c) and 20 μm (d-m).

Figure 4. A GA signalling activity map reveals high levels of GA signalling activity in inter-primordia cells in the SAM.

a, Maximum intensity projection showing the expression of *pRPS5a::qRGA*^{mPFYR} and *pCLV3::mCherry-NLS* in the SAM (overlay). CZ, central zone; P, primordium. **b**, Heatmap representation of L1 GA signalling activity averaged from seven SAMs aligned using the CLV3 domain as a reference. **c-d**, Quantification of GA signalling activity in central zone (CZ), inter-primordia region (IPR) and primordia (P) indicated by different colours as shown in (**c**). *P* values are from one way ANOVA. **e,** 3D visualization of nlsGPS1 emission ratio in the SAM. Primordia stages are estimated according to morphology. Arrows highlight higher nlsGPS emission ratio in the boundaries and IPR. **f-g,** Fluorescence distribution in wild-type (L*er*) SAMs treated with fluorescein (Fl, **f**) and GA_4-Fl (**g**). The inserts show the same images merged with the PI channel that visualizes cell membranes (magenta). **h**, Comparison of the ratio of average fluorescence intensity in the IPR to that in the non-IPR (excluding primordia)

between Fl and GA_4-Fl treatment in the SAM. *P* value is from a Wilcoxon rank-sum test. The experiment was repeated twice with similar results. Scale bars = 20 µm.

Extended data Figure 7. Digital longitudinal sections through the centre of the SAM and primordia of qRGA^{mPFYR} plants.

a, Maximum intensity projection showing the expression of *pRPS5a::qRGA^{mPFYR} pCLV3::mCherry-NLS* plants in the SAM as in Fig 4a. CZ, central zone. **b**, Signals for qRGA^{mPFYR}-VENUS, TagBFP-NLS and mCherry-NLS in digital longitudinal sections through the centre of CZ and primordia P_1 to P_8 along the white dotted lines indicated in (**a**). Scale bars = 20 µm.

Extended data Figure 8. Response of nlsGPS1 to GA treatment in the SAM.

a-d, 3D visualization of nlsGPS1 expression in the SAM before (**a**, **c**) and after (**b**, **d**) mock (**a**, **b**) and 10 µM GA_{4+7} treatment (**c**, **d**). **e**, Boxplot representation of nlsGPS1 emission ratios from nuclei analysed in three SAMs. The number of nuclei N is indicated. *P* value is from a Wilcoxon rank-sum test. The experiment was repeated twice with similar results.

Extended data Figure 9. Fluorescence distribution in SAMs treated with Fl and GA_3-, GA_4- and GA_7-Fl.

a-b, Fluorescence distribution in wild-type (L*er*) SAMs treated with GA_3-Fl (**a**) and GA_7-Fl (**b**). The inserts show the same images overlaid with the PI channel that visualizes cell membrane (magenta). **c**, Ratio of average fluorescence intensity in the IPR to that in the non-IPR (excluding primordia) after GA_3-Fl and GA_7-Fl treatment in the SAM, compared to Fl treatment (Fig 4f, h). *P* values are from Wilcoxon rank-sum tests. **d-g,** Digital longitudinal sections through the centre of CZ and primordia P_3 to P_7 of L*er* SAMs treated with 5 µM

fluorescein (**d**), GA_3-Fl (**e**), GA_4-Fl (**f**), or GA_7-Fl (**g**) (green) and stained with PI (red). Scale bars = 20 μm.

Figure 5. High GA signalling activity correlates positively with growth anisotropy and transverse cell division orientation.

a-b, Averaged surfacic growth (**a**) and growth anisotropy (**b**) heat maps (used as proxies for cell expansion intensity and direction, respectively) in the SAM. **c**, PCA analysis including the following variables: GA signalling, surfacic growth intensity, surfacic growth anisotropy and CLV3 expression. **d**, Spearman correlation study between GA signalling, surfacic growth intensity and surfacic growth anisotropy in tissue scale but excluding CZ. **e**, 3D visualization of Col-0 SAM L1 cells using confocal microscopy. New cell walls formed in the SAM (but not primordia) in 10 h are coloured according to their angle values. The insert shows the corresponding 3D image at 0 h. **f**, Boxplot representation of cell division frequency in the IPR and non-IPR of Col-0 SAM. *P* value is from Wilcoxon rank-sum test. **g**, A schematic diagram showing how the angle of a new cell wall (magenta) relative to the radial direction from the centre of the SAM (white dotted line) was measured. Only acute angle values (i.e: 0-90°) are considered. **h**, Frequency histograms of division plane orientation of cell from the entire SAM (dark blue), the IPR (medium blue) and non-IPR (light blue), respectively. **i**, Frequency histograms of division plane orientation of cells located in front and sides of P_3 (light green), P_4 (mediate green) and P_5 (dark green), respectively. *P* values are from Kolmogorov-Smirnov tests. The experiment was repeated twice with similar results.

Extended Data Figure 10. Expression patterns of DELLA-encoding genes and DELLA proteins in the SAM.

a-d, GUS signal in the shoot apex of *pGAI::GUS* (**a**), *pRGA::GUS* (**b**), *pRGL1::GUS* (**c**) and *rgl2-5* (a promoter trap GUS line) mutant (**d**). **e-h**, *In situ* hybridization serial sections through a shoot apex using probes of GAI (**e**), RGL1 (**f**), RGL2 (**g**) and RGL3 (**h**). **i-j,** Intensity heatmaps of maximum intensity-projection of *pRGL3::RGL3-GFP* (**i**) and *pRGA::GFP-RGA* (**j**) in the SAM. Arrowheads mark the regions with lower GFP-RGA expression. Scale bars = 20 µm.

Figure 6. Cell division orientation distribution in the SAM are modified in global *della* mutant and *pCUC2::gai-1-VENUS* transgenic plant.

a-b, 3D visualisation of the L1 layer of PI-stained L*er* (**a**) and global *della* mutant (**b**) SAM using confocal microscopy. New cell walls formed in the SAM but not primordia in 10 h are shown and coloured according to their angle values. Inserts show the SAM at 0 h. Arrows in (**b**) highlight examples of aligned cell files in global *della* mutant. **c-e**, Comparison of frequency distribution of division plane orientation of cells in the entire SAM (**d**), IPR (**e**) and non-IPR (**f**) between L*er* and global *della*. *P* values are from Kolmogorov-Smirnov tests. The experiment was repeated three times with similar results. **f-g**, 3D visualisation of confocal image stacks of PI-stained SAMs of Col-0 (**i**) and *pCUC2::gai-1-VENUS* (**j**) transgenic plants. New cell walls formed in the SAM but not primordia in 10 h are shown as in (**a**,**b**). **h-j**, Comparison of frequency distribution of division plane orientation of cells located in the entire SAM (h), IPR (i) and non-IPR (j) between Col-0 and *pCUC2::gai-1-VENUS* transgenics. *P* values are from Kolmogorov-Smirnov tests. The experiment was repeated three times with similar results.

Extended Data Figure 11. Analysis of SAM shape of global and quadruple *della* mutants and *pCUC2::gai-1-VENUS* transgenic plants.

a-c, Maximum projection (**a-c**) and orthogonal views (XZ dimension, lower panels**;** YZ dimension, left panels) of PI-stained SAMs of L*er* (**a**), global *della* (**b**) and quadruple *della* mutant (**c**) using confocal microscopy. **d**, Comparison of SAM size between L*er*, global and quadruple *della* mutants. *P* values are from Kruskal-Wallis tests. **e**,**f**, XZ point plots of L1 nuclei of L*er* (blue), global *della* (orange) and quadruple *della* (green) showing the tissue-level curvature of the SAM. **g-j**, Heatmaps of cellular curvature of L1 cells in the SAM (including P_4) of L*er* (**g**), global *della* (**h**) and quadruple *della* (**i**). Statistics are shown in (**j**). *P* values are from Kruskal-Wallis tests. **k**, Maximum projection view of the SAM of *pCUC2::LSSmOrange-NLS* line. The insert shows the same image superimposed with the expression of *pRPS5a::TagBFP-NLS*. **l-m**, Maximum projection (**l-m**) and orthogonal views (XZ dimension, lower panels**;** YZ dimension, left panels) of PI-stained SAM of *pCUC2::gai-1-VENUS* (**m**) transgenic plant and its wild-type control (**l**). **n**, XZ point plots of L1 nuclei of wild-type (blue) and *pCUC2::gai-1-VENUS* transgenic plants (yellow) showing the tissue-level curvature of the SAM. **o-q**, Heatmaps of cellular curvature of L1 cells in the SAM of wild-type (**o**) and *pCUC2::gai-1-VENUS* (**p**) transgenic plants. Statistics are shown in (**q**). *P* value is from Wilcoxon rank-sum test. Scale bars = 20 μm.

Extended Data Figure 12. Cell division plane orientation distribution in the SAM of quadruple *della* mutants.

a-b, 3D visualization of the L1 of PI-stained SAM of quadruple *della* mutant using confocal microscopy. New cell walls formed in the SAM (but not in primordia) in 10 h are shown and coloured according to their angle values. (**a**) is representative of 6 out of 13 SAMs while (**b**) represents the remaining 7 SAMs where a higher frequency of transverse cell divisions could be detected. Inserts are images at 0 h. (**c**) Comparison of frequency distributions of division

plane orientation between cells located in the entire SAM of L*er* and quadruple *della* mutants. *P* value is from Kolmogorov-Smirnov test.

Figure 7. Emergence of the internode cellular organisation in the inter-primordia region in wild-type and in plants with modified GA signalling activity.

a-l, Time-lapse (0 h, 24 h, 34 h) visualization of the L1 of the SAM from confocal mciroscopy of L*er* (**a-c**), global *della* (**d-f**), Col-0 (**g-i**) and *pCUC2::gai-1-VENUS* transgenic (**k-n**). The imaging time is indicated at the right up corner of each panel. Cells outlined with yellow dotted lines are those incorporated into a primordium at 34 h, and cells in green are found in the IPR at 34 h. Those in orange produce both primordium and IPR cells. White dotted lines mark the edge of the elder primordium (that have been removed at 34h except in (**c**)). **m-p,** Scanning electron microscopy images the shoot apex of L*er* (**m**), global *della* (**n**), Col (**o**), and *pCUC2::gai-1-VENUS* (**p**) allowing to analyse the early establishment of internode just below the SAM. The different size of arrows indicates different range of size of the early internode in the different genetic background.

Extended Data Figure 13. Altered plant height in *pCUC2::gai-1-VENUS* transgenic plants.

Representative 37-d-old wild-type (**a**) and 56-d-old *pCUC2::gai-1-VENUS* transgenic plants (**b**) grown under long-day conditions. Scale bars = 1 cm.

Extended Data Figure 14. Hypothesis of the role of GA signalling in internode specification.

Higher levels of GA signalling activity in the IPR specify the cellular organization of internode in the SAM via a regulation on cell division orientation.

Acknowledgments

We thank the colleagues of the Laboratoire Reproduction et Développement des Plantes for fruitful discussions on this work and for sharing material and advice. We also thank Miguel Perez-Amador, Jan Lohmann, Yvon Jaillais, Tai-ping Sun, Miguel Blazquez, David Alabadi and the NASC for seeds and plasmids. We acknowledge the contribution of SFR Biosciences (UMS3444/CNRS, US8/Inserm, ENS de Lyon, UCBL) facility PLATIM for assistance with microscopy and image analysis. This work was supported by the ANR-16-CE13-0014 (GrowthDynamics) grant to T.V. and P.A; a European Research Council grant (GAtransport) to R.W..

Author contribution

P.A. and T.V. designed the study and supervised the work; B.S., A.F.-B., P.A. and T.V. designed the experiments. B.S., A.W. and A.M. performed the FRET analysis; A.N.-G. and S.P. conducted the large-scale two-hybrid analysis; S.L. and R.W. designed the synthesis strategy and synthesized the GA-fl fluorescent probes. G.C. developed the pipeline for quantitative image analysis with the help of J.L.; B.S., A.F.-B., and G.C. performed the image analysis. B.S., A.F.-B., C.G.-A., L.J., G.B., J.M., L.S.-A. and J.-M.D. performed all the other experiments; all authors were involved in data analysis; B.S., A.F.-B., P.A. and T.V. wrote the manuscript with inputs from all authors.

Financial competing interests

The authors declare no competing interests.

Corresponding authors

Correspondence and request for materials should be addressed to T.V. (teva.vernoux@ens-lyon.fr) or P.A. (patrick.achard@ibmp-cnrs.unistra.fr).

Data and software availability

All experimental data and quantified data that support the findings of this study are available from the corresponding authors upon request. Quantitative image and geometry analysis algorithms are provided in Python libraries timagetk, cellcomplex, tissue_nukem_3d and sam_atlas (https://gitlab.inria.fr/mosaic/) made publicly available under the CECILL-C license. The script used to process hypocotyl images is publicly available in the qrga_nuclei_quantification project (https://gitlab.inria.fr/gcerutti/). The pipelines used to analyze SAM image sequences and to produce map visualizations are provided in a separate project (https://gitlab.inria.fr/mosaic/publications/sam_spaghetti) as Python scripts.

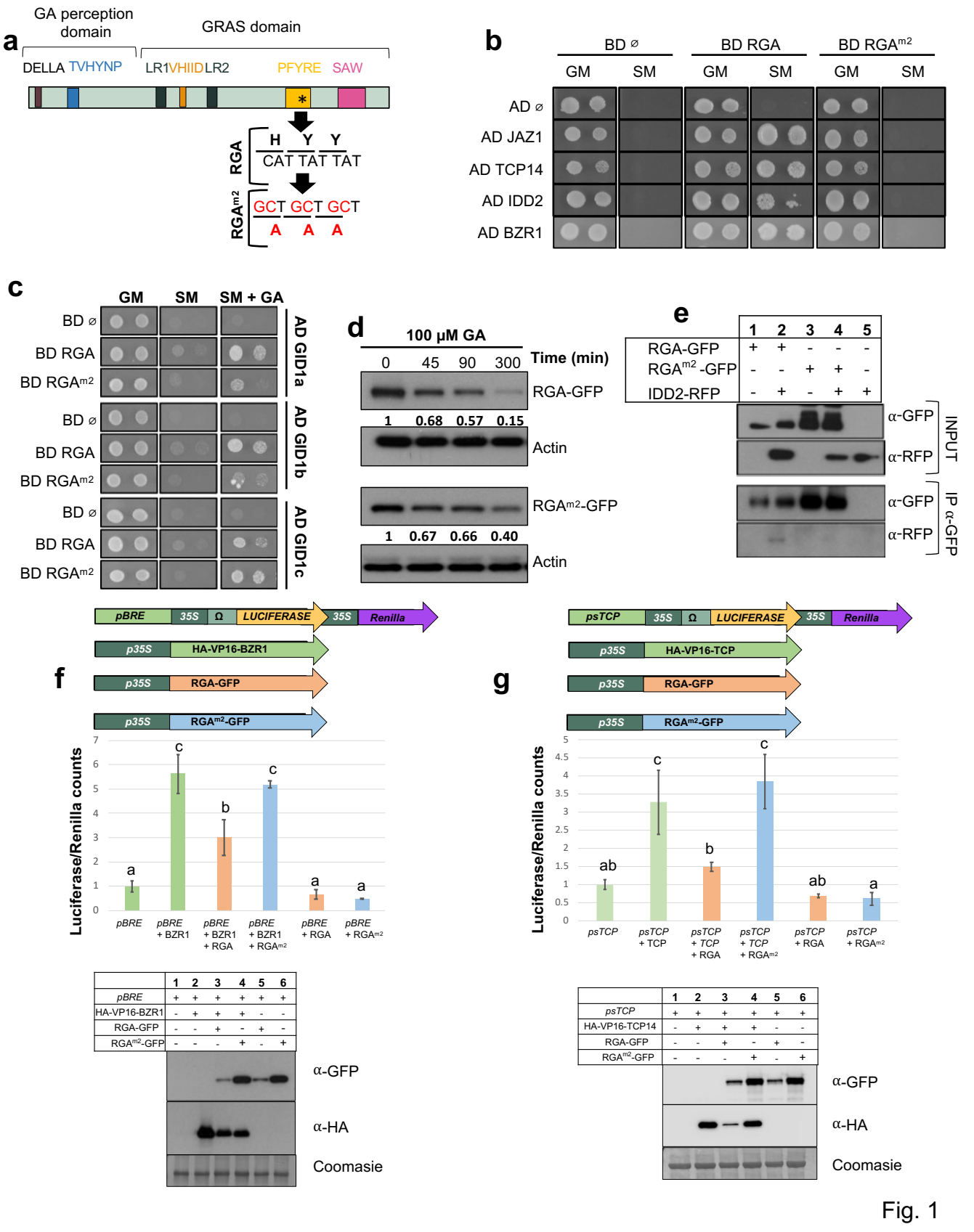
a
GA perception domain
GRAS domain
DELLA TVHYNP
LR1VHIID LR2
PFYRE SAW
RGA
H Y Y
CAT TAT TAT
RGAm2
GCT GCT GCT
A A A
b
BD ∅
BD RGA
BD RGAm2
GM SM GM SM GM SM
AD ∅
AD JAZ1
AD TCP14
AD IDD2
AD BZR1
c
GM SM SM + GA
BD ∅
BD RGA
BD RGAm2
AD GID1a
AD GID1b
AD GID1c
d
100 µM GA
0 45 90 300 Time (min)
RGA-GFP
1 0.68 0.57 0.15
Actin
RGAm2-GFP
1 0.67 0.66 0.40
Actin
e
1 2 3 4 5
RGA-GFP + + - - -
RGAm2-GFP - - + + -
IDD2-RFP - + - + +
α-GFP
α-RFP
INPUT
IP α-GFP
f
pBRE 35S Ω LUCIFERASE 35S Renilla
p35S HA-VP16-BZR1
p35S RGA-GFP
p35S RGAm2-GFP
Luciferase/Renilla counts
pBRE
pBRE + BZR1
pBRE + BZR1 + RGA
pBRE + BZR1 + RGAm2
pBRE + RGA
pBRE + RGAm2
1 2 3 4 5 6
pBRE + + + + + +
HA-VP16-BZR1 - + + + - -
RGA-GFP - - + - + -
RGAm2-GFP - - - + - +
α-GFP
α-HA
Coomasie
g
psTCP 35S Ω LUCIFERASE 35S Renilla
p35S HA-VP16-TCP
p35S RGA-GFP
p35S RGAm2-GFP
Luciferase/Renilla counts
psTCP
psTCP + TCP
psTCP + TCP + RGA
psTCP + TCP + RGAm2
psTCP + RGA
psTCP + RGAm2
1 2 3 4 5 6
psTCP + + + + + +
HA-VP16-TCP14 - + + + - -
RGA-GFP - - + - + -
RGAm2-GFP - - - + - +
α-GFP
α-HA
Coomasie

Fig. 1

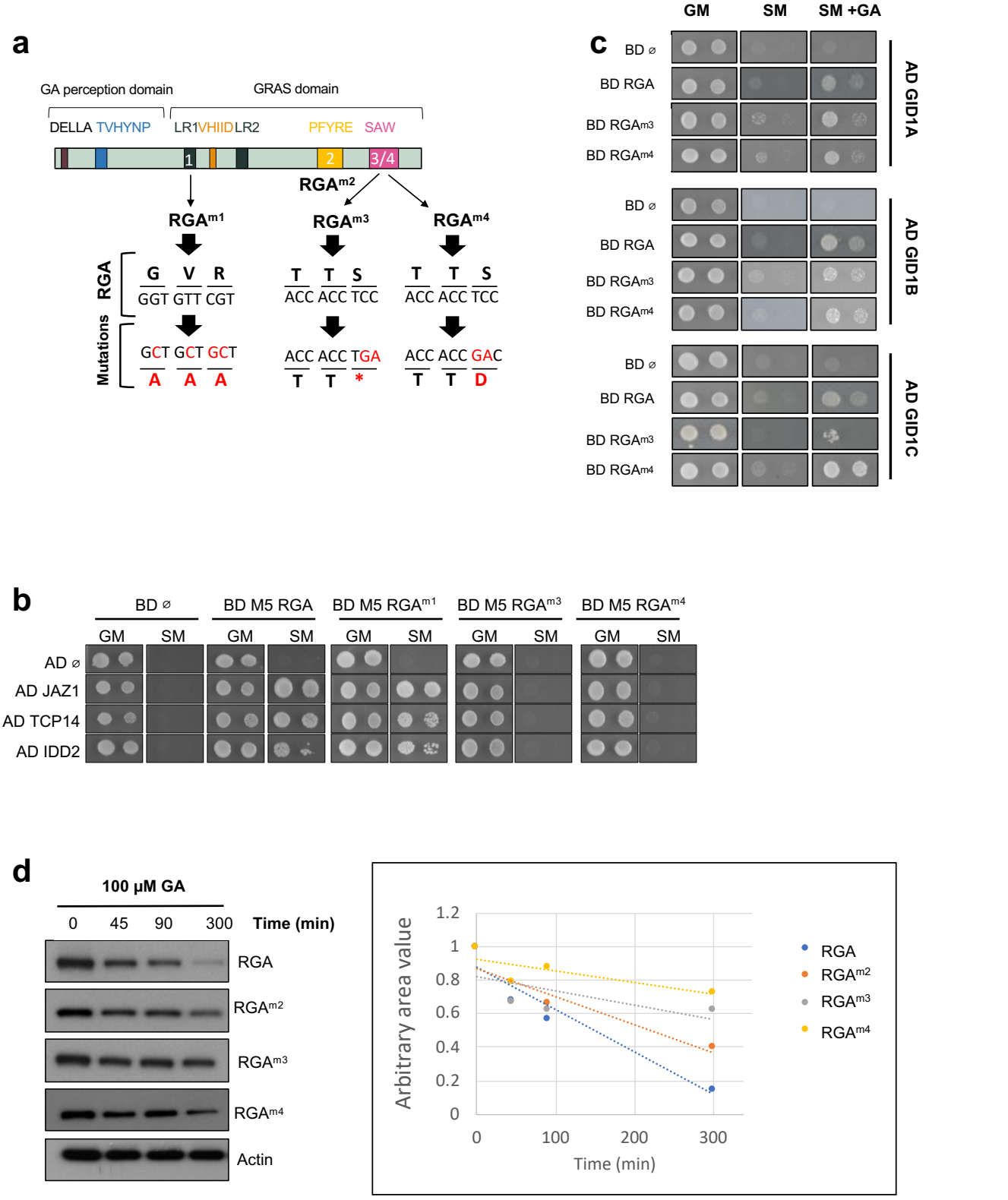

Extended Data Fig. 1

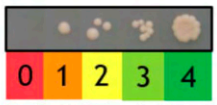

Intensity of the interaction

Plate-Position in MINILIBRARY	AGI	TF Name	Interaction in - LWH			
			GAI	RGA	RGA^{m2}	ø
002-A01	At2g31380	STH	4	0	0	0
002-A02	At5g25810	ERF040/TINY	4	0	0	0
002-A03	At1g27050	HB54	4	0	0	0
002-A04	At5g66700	HB-8/HB-53	4	0	1	0
002-A05	At2g31380	STH	4	0	0	0
002-A06	At2g28910	CXIP4	4	0	0	0
002-A07	At4g21040	DOF4.3	4	0	0	0
002-A08	At4g01350	DC1	4	0	0	0
002-A09	At4g01350	DC1	4	0	0	0
002-A10	At2g02080	ATIDD4	4	4	0	0
002-A11	At4g03250	HDZIP	4	0	0	0
002-A12	At4g03250	HDZIP	4	0	0	0
002-B01	At4g17460	HAT1	4	0	0	0
002-B02	At3g04420	ANAC048	4	1	0	0
002-B03	At1g73100	SUVH3	3	0	0	0
002-B04	At3g02310	AGL4/SEP2	4	0	0	0
002-B05	At1g17590	NFYA8	4	0	0	0
002-B06	At1g77920	bZIP50/TGA7	3	0	0	0
002-B07	At5g06839	bZIP65/TGA10	4	0	0	0
002-B08	At1g25340	MYB116	3	0	0	0
002-B09	At5g35550	TT2/MYB123	4	0	0	0
002-B10	At4g22680	MYB85	4	0	1	0
002-B11	At5g62320	MYBCU15/MYB99	4	0	0	0
002-B12	At5g62320	MYBCU15/MYB99	4	0	0	0
002-C01	At1g17770	SUVH7/SDG17/SET17	4	0	0	0
002-C02	At1g09540	MYB61	4	4	0	0
002-C03	At2g36890	BIT1/MYB38/RAX2	4	0	0	0
002-C04	At5g12870	MYB46	4	1	0	0
002-C05	At3g09600	RVE8/LCL5	4	0	0	0
002-C06	At3g09600	RVE8/LCL5	3	1	0	0
002-C07	At4g24240	WRKY7	4	4	0	0
002-C08	At4g22070	WRKY31	4	3	0	0
002-C09	At1g69810	WRKY36	4	1	0	0
002-C10	At5g24520	TTG1	4	1	0	0
002-C11	At3g47620	TCP14	4	1	0	0
002-C12	At1g69690	TCP15	4	0	0	0
002-D01	At1g31630	AGL86	4	0	0	0
002-D02	At5g26650	AGL36	4	1	0	0
002-D03	At1g22590	AGL87	4	0	0	0
002-D04	At2g24430	ANAC038	4	1	0	0
002-D05	At2g45050	GATA2	3	0	0	0
002-D06	At3g21175	GATA24/ZML1	4	0	0	0
002-D07	At1g24625	ZFP7	4	2	0	0
002-D08	At2g41940	ZFP8	4	2	0	0
002-D09	At4g16610	C2H2	3	0	0	0
002-D10	At5g43700	AUX2-11/IAA4	3	0	0	0
002-D11	At3g23050	IAA7	3	0	0	0
002-D12	At3g02150	TCP13	4	3	0	0
002-E01	At2g24430	ANAC038	4	0	0	0
002-E02	At2g45050	GATA2	4	0	0	0
002-E03	At1g70000	myb-type HTH	4	0	0	0
002-E04	At3g20310	ERF083/ERF7	4	3	1	1
002-E05	At5g18560	PUCHI/ERF086	4	0	0	0
002-E06	At1g49480	REM19/RTV1	4	1	1	0
002-E07	At1g14600	Homeodomain/G2-like?	4	0	1	0
002-E08	At5g16560	KAN1	4	1	0	0
002-E09	At5g05090	Homeodomain/G2-like?	4	2	0	0
002-E10	At1g51140	bHLH122/EN70/ Flowering bHLH3/FBH3	4	4	0	0
002-E11	At2g42280	Flowering bHLH4/ FBH4	4	0	0	0
002-E12	At1g61660	bHLH112/EN64	4	3	0	0
002-F01	At5g64750	ABR1/ERF111	4	1	0	0
002-F02	At5g54070	HSFA9	4	0	0	0
002-F03	At5g09460	bHLH143/EN129/AJAX3	4	0	0	0
002-F04	At1g19210	ERF017	4	0	0	0
002-F05	At5g17690	LHP1/TFL2	3	1	0	0
002-F06	At4g13980	HSF12/HSFA5	4	1	0	0
002-F07	At2g01760	ARR14	3	0	0	0
002-F08	At2g31220	bHLH10/EN23	4	0	0	0
002-F09	At4g02590	bHLH59/UNE12	4	0	0	0
002-F10	At4g30935	WRKY32	4	4	1	0
002-F11	At1g68920	bHLH49/EN82	4	1	0	0
002-F12	At2g40340	ERF48/DREB2C	4	0	0	0
002-G01	At3g09600	RVE8/LCL5	4	0	0	0
002-G02	At1g51600	GATA28/ZML2	4	0	0	0
002-G03	At3g29035	NAC3/ANAC059/ORS1	4	3	0	0
002-G04	At5g66700	HB-8/HB-53	3	0	0	0
002-G05	At4g37750	ANT	4	3	0	0
002-G06	At5g60120	TOE2	4	1	0	0
002-G07	At1g43160	RAP2-6/ERF108	4	0	0	0
002-G08	At1g77200	ERF037	4	1	0	0
002-G09	At3g57600	DREB2F	4	0	0	0
002-G10	At2g28910	CXIP4	4	0	0	0
002-G11	At2g28910	CXIP4	4	0	0	0
002-G12	At1g31630	AGL86	4	0	0	1
002-H01	At5g26650	AGL36	4	0	0	0
002-H02	At1g69690	TCP15	4	1	0	0
002-H03	At3g47620	TCP14	4	0	0	0
002-H04	At5g29000	PHL1	4	0	0	0
002-H05	No gene	Control	4	0	0	0
002-H06	At1g09530	bHLH8/EN100/PIF3	4	4	0	0
002-H07	At2g43010	SRL2/PIF4	4	0	0	0
002-H08	At2g33880	HB-3/STIP/WOX9A	4	3	0	0

Extended Data Fig. 2

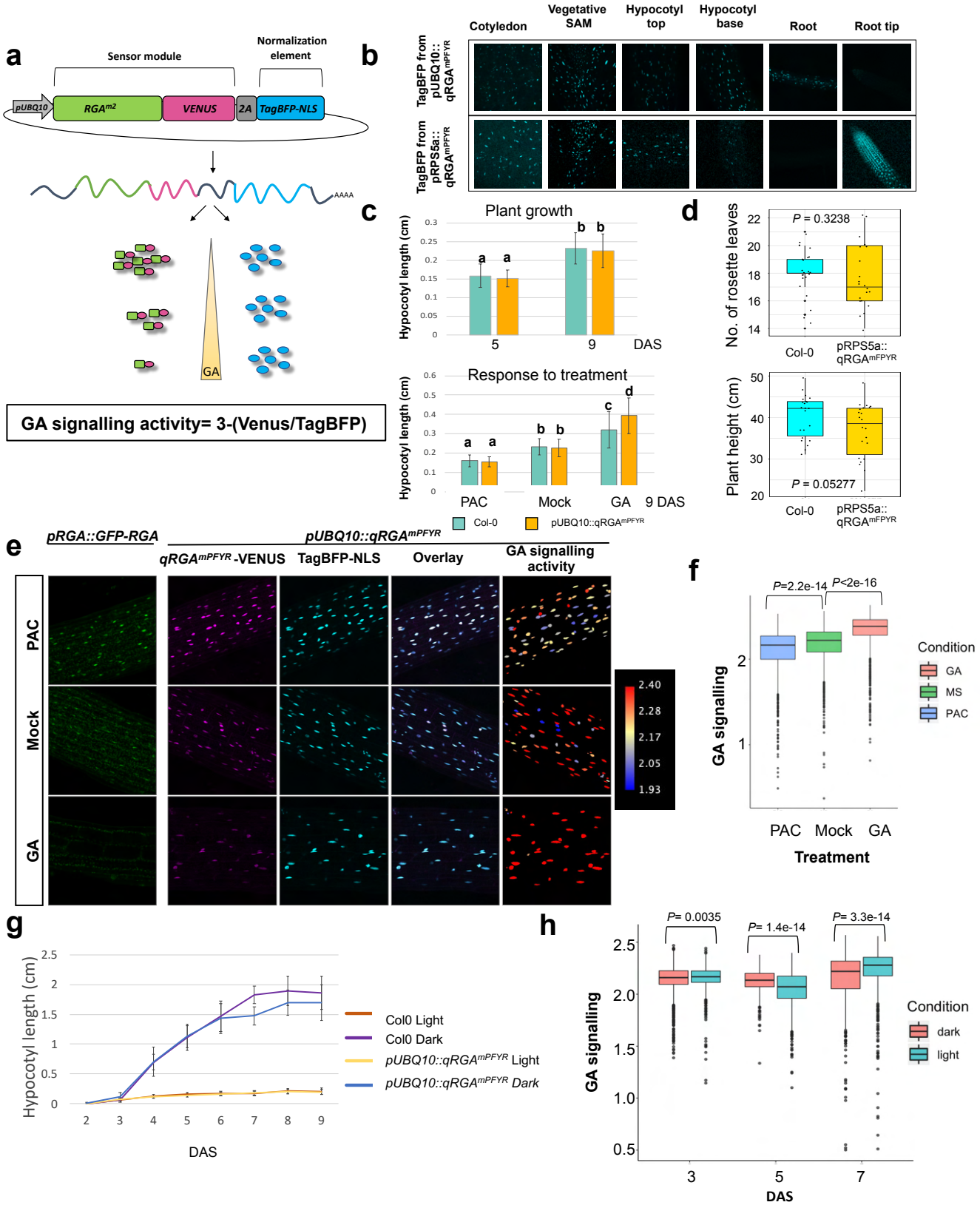
a
Sensor module
Normalization element
pUBQ10
RGAm2
VENUS
2A
TagBFP-NLS
AAAA
GA
GA signalling activity= 3-(Venus/TagBFP)
b
Cotyledon
Vegetative SAM
Hypocotyl top
Hypocotyl base
Root
Root tip
TagBFP from pUBQ10::qRGAmPFYR
TagBFP from pRPS5a::qRGAmPFYR
c
Plant growth
Hypocotyl length (cm)
DAS
Response to treatment
PAC
Mock
GA
9 DAS
Col-0
pUBQ10::qRGAmPFYR
d
No. of rosette leaves
P = 0.3238
Col-0
pRPS5a::qRGAmPFYR
Plant height (cm)
P = 0.05277
e
pRGA::GFP-RGA
pUBQ10::qRGAmPFYR
qRGAmPFYR-VENUS
TagBFP-NLS
Overlay
GA signalling activity
PAC
Mock
GA
2.40
2.28
2.17
2.05
1.93
f
P=2.2e-14
P<2e-16
GA signalling
Condition
GA
MS
PAC
PAC
Mock
GA
Treatment
g
Hypocotyl length (cm)
DAS
Col0 Light
Col0 Dark
pUBQ10::qRGAmPFYR Light
pUBQ10::qRGAmPFYR Dark
h
P= 0.0035
P= 1.4e-14
P= 3.3e-14
GA signalling
Condition
dark
light
DAS

Fig. 2

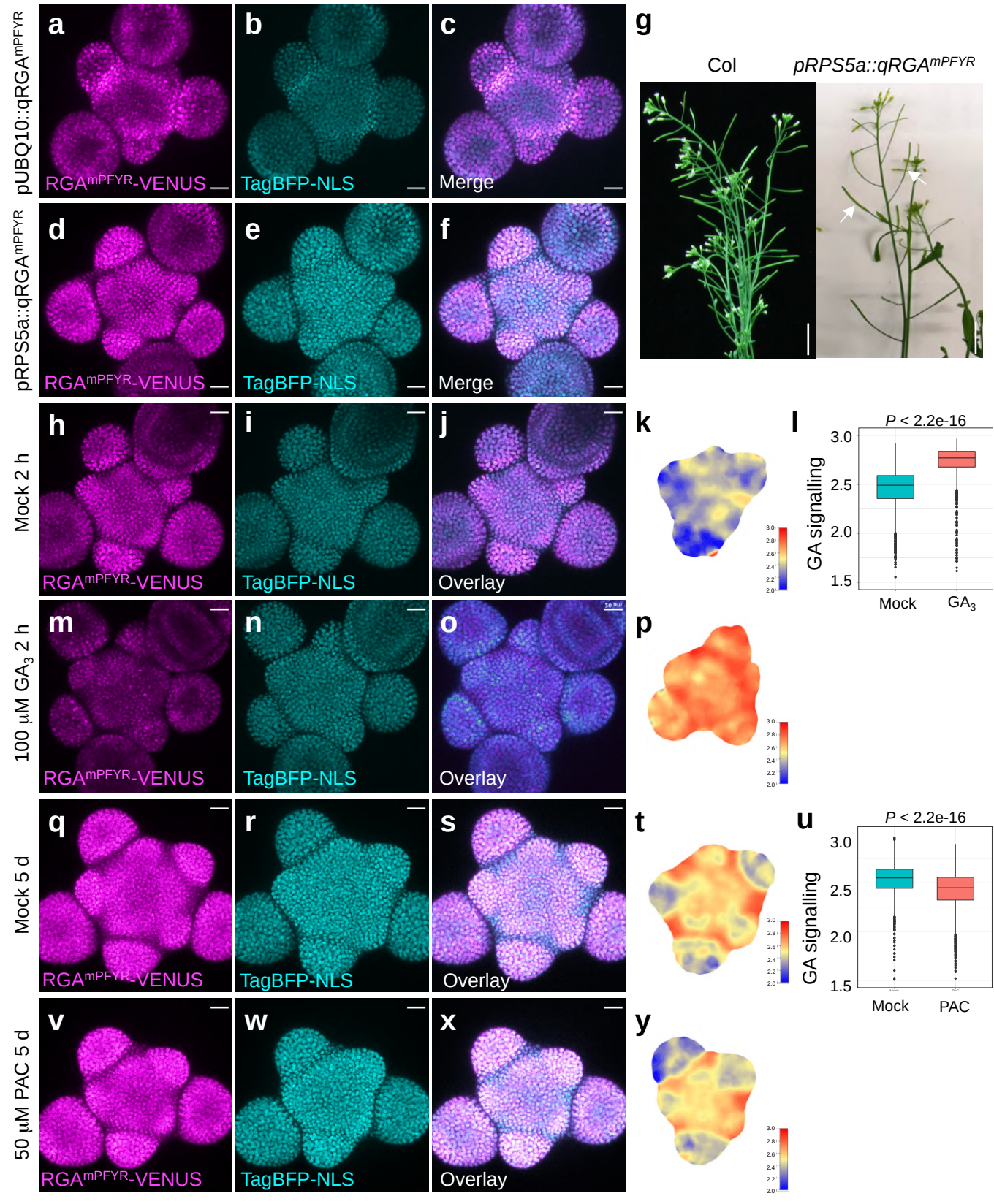

Extended data Fig. 3

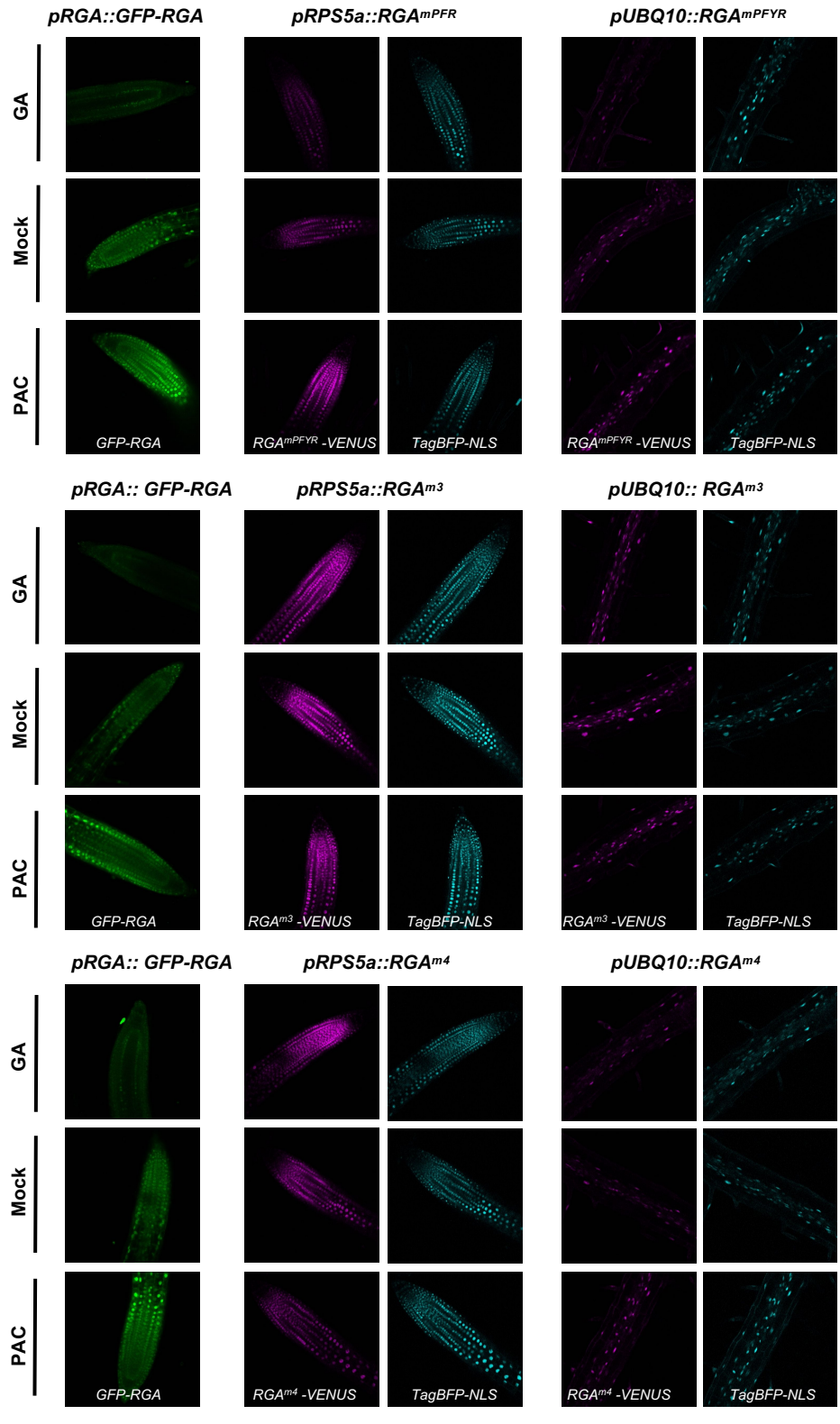

Extended Data Fig. 4

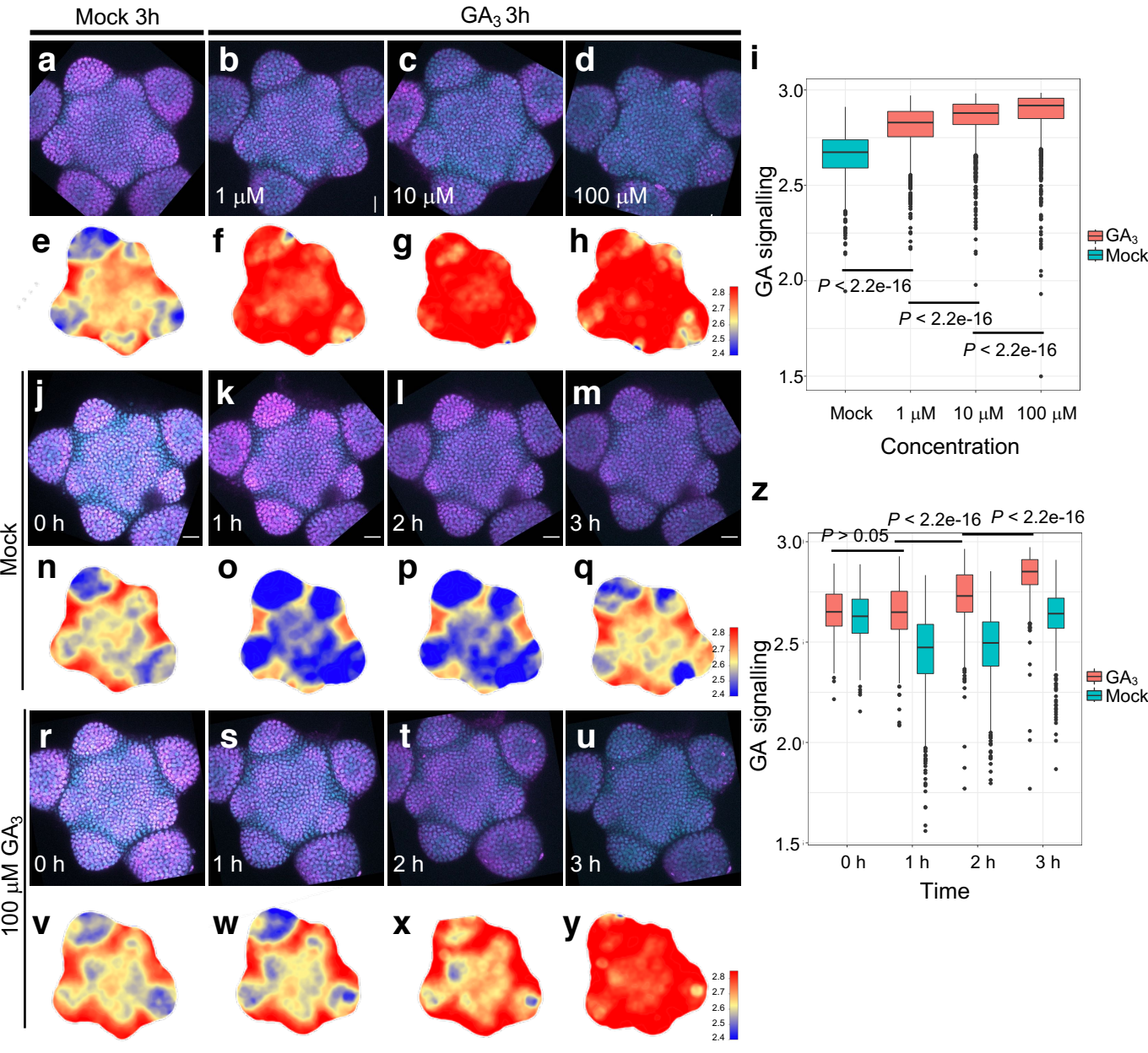

Extended data Fig. 5

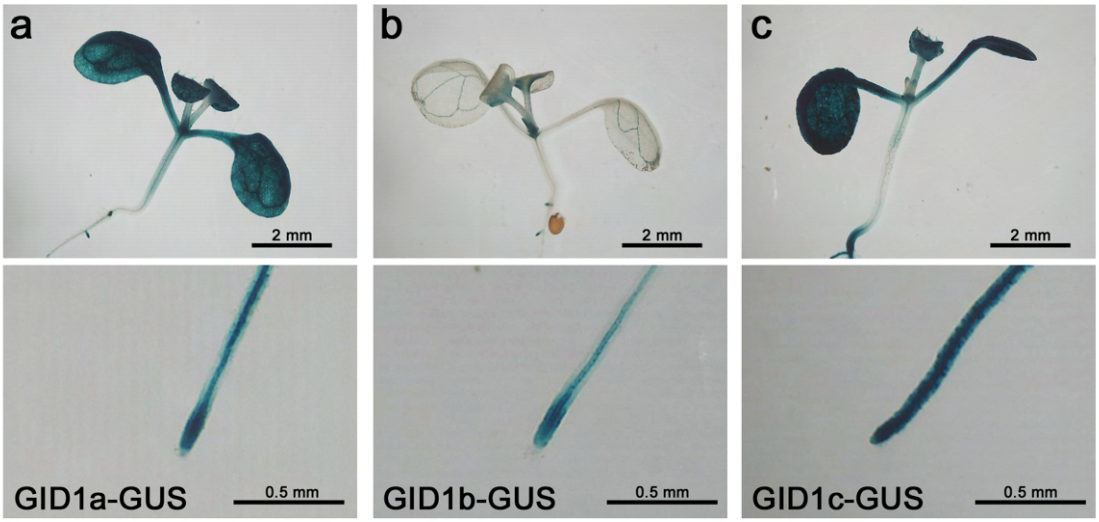
a
b
c
2 mm
2 mm
2 mm
GID1a-GUS
0.5 mm
GID1b-GUS
0.5 mm
GID1c-GUS
0.5 mm

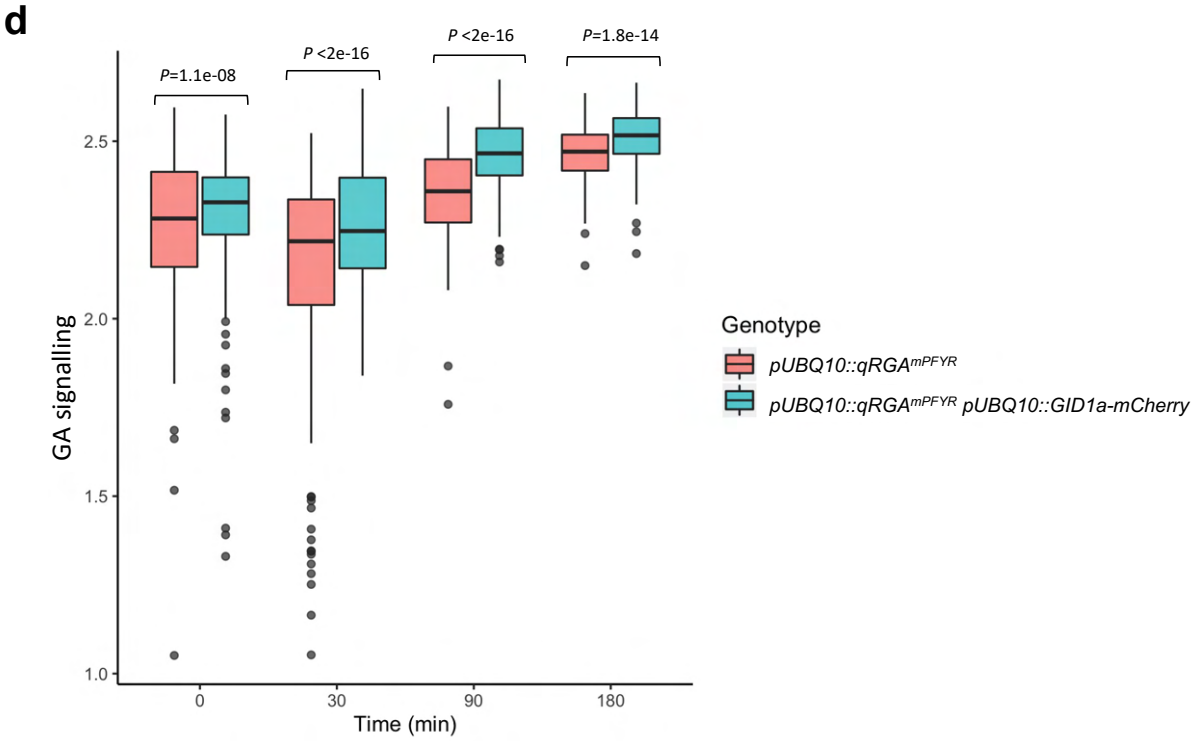
d
P=1.1e-08
P <2e-16
P <2e-16
P=1.8e-14
GA signalling
2.5
2.0
1.5
1.0
0
30
90
180
Time (min)
Genotype
pUBQ10::qRGA^mPFYR
pUBQ10::qRGA^mPFYR pUBQ10::GID1a-mCherry

Fig. 3

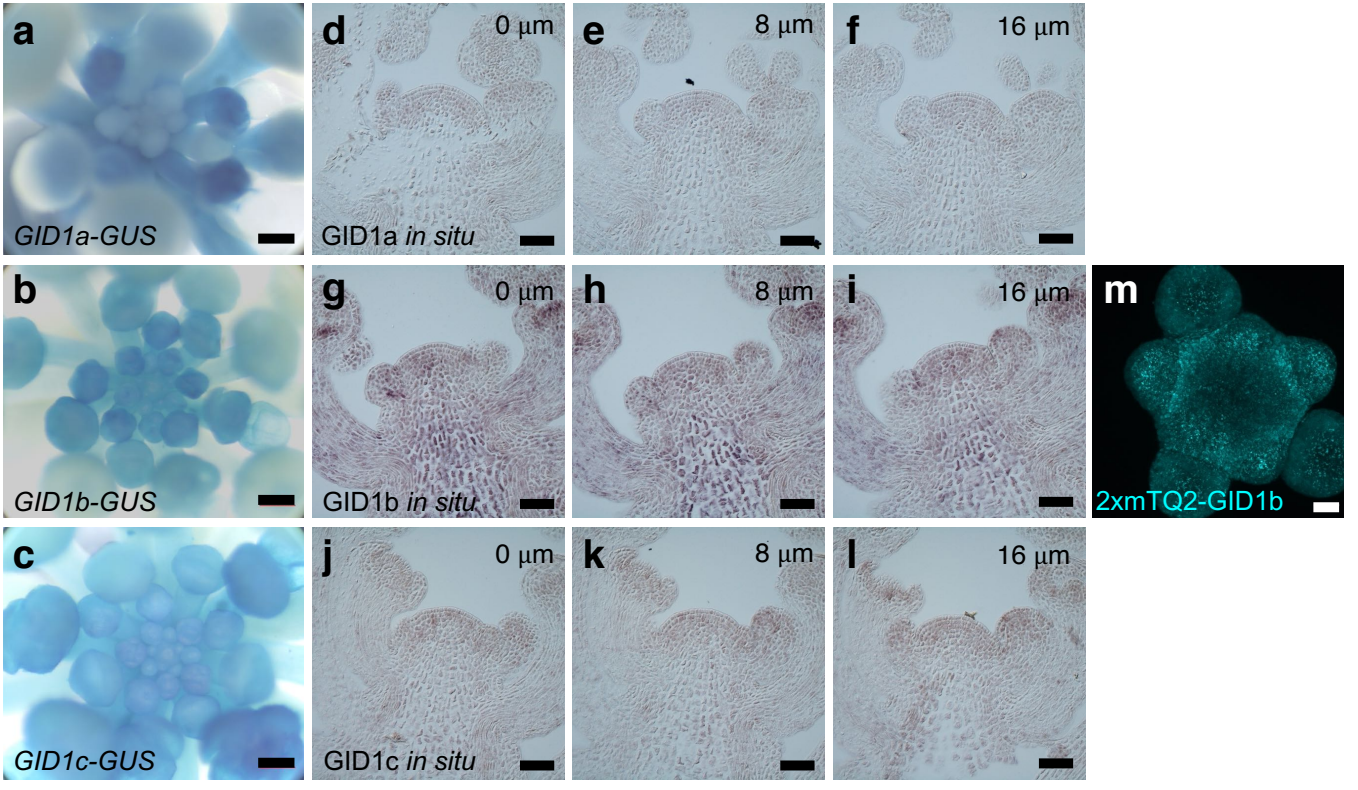

Extended data Fig. 6

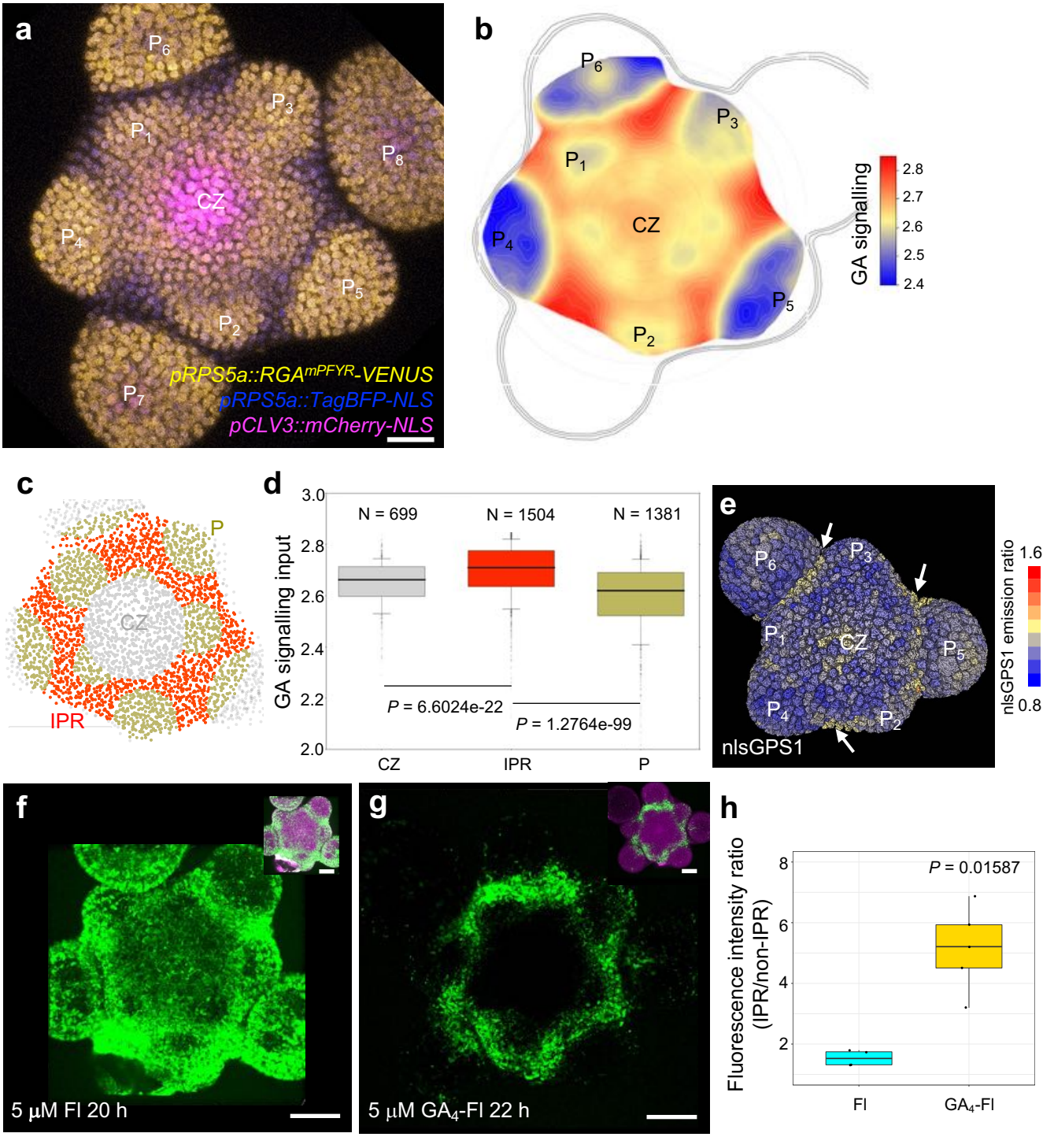
a
P6
P3
P1
P8
CZ
P4
P5
P2
P7
pRPS5a::RGAmPFYR-VENUS
pRPS5a::TagBFP-NLS
pCLV3::mCherry-NLS
b
P6
P3
P1
CZ
P4
P5
P2
GA signalling
2.8
2.7
2.6
2.5
2.4
c
P
CZ
IPR
d
N = 699
N = 1504
N = 1381
GA signalling input
3.0
2.8
2.6
2.4
2.2
2.0
P = 6.6024e-22
P = 1.2764e-99
CZ
IPR
P
e
P6
P3
P1
CZ
P5
P4
P2
nlsGPS1
nlsGPS1 emission ratio
1.6
0.8
f
5 µM FI 20 h
g
5 µM GA4-FI 22 h
h
Fluorescence intensity ratio (IPR/non-IPR)
8
6
4
2
P = 0.01587
FI
GA4-FI

Fig. 4

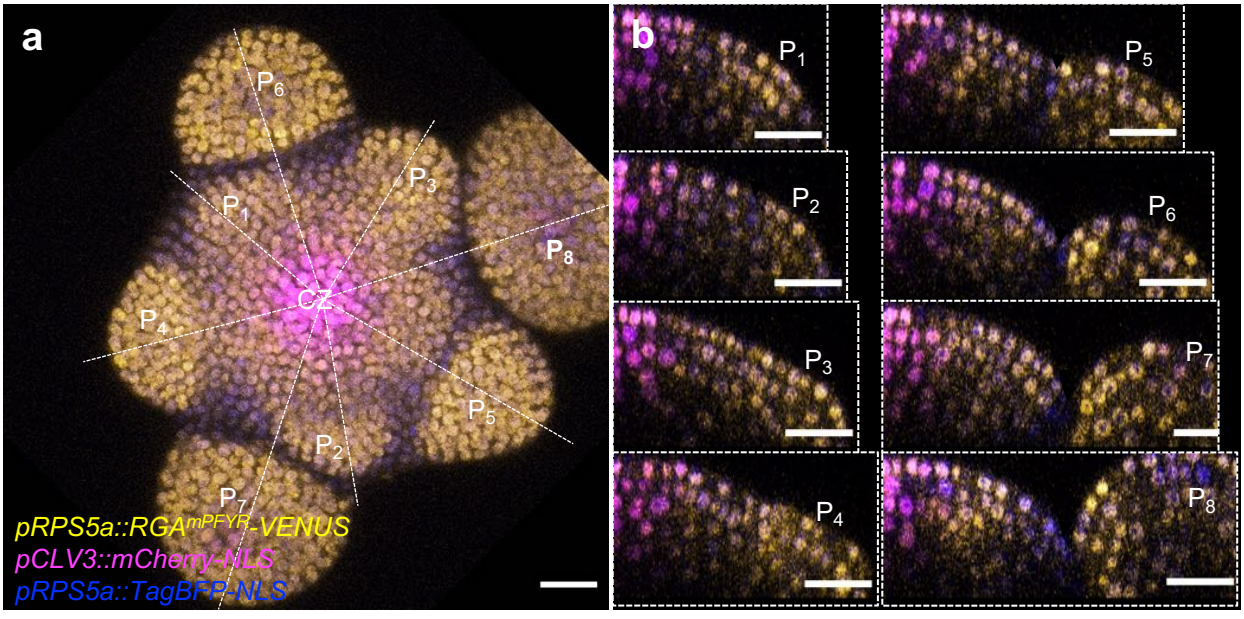

Extended data Fig. 7

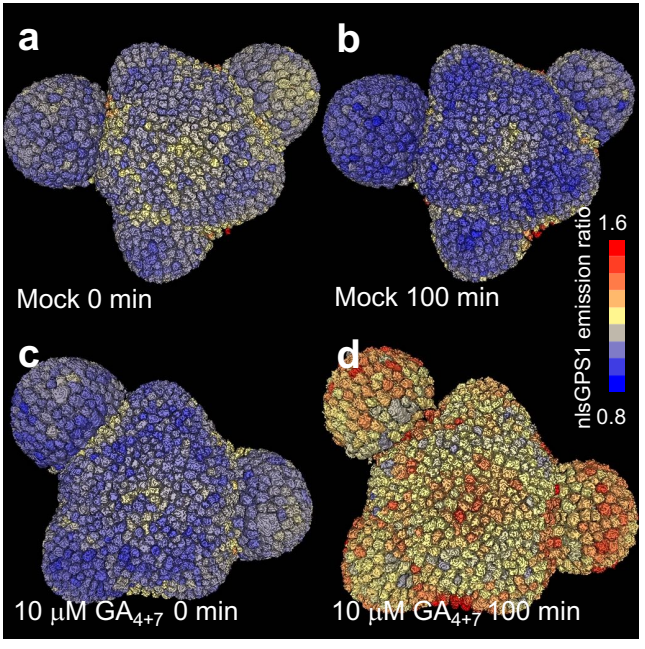

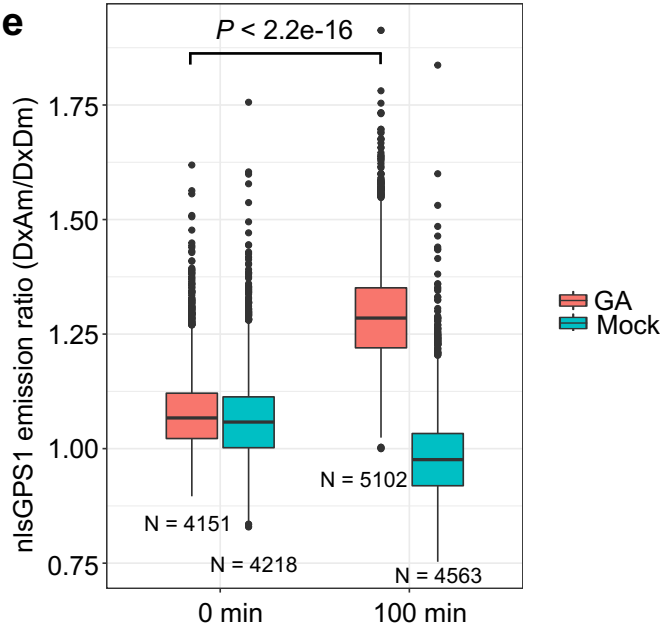

Extended data Fig. 8

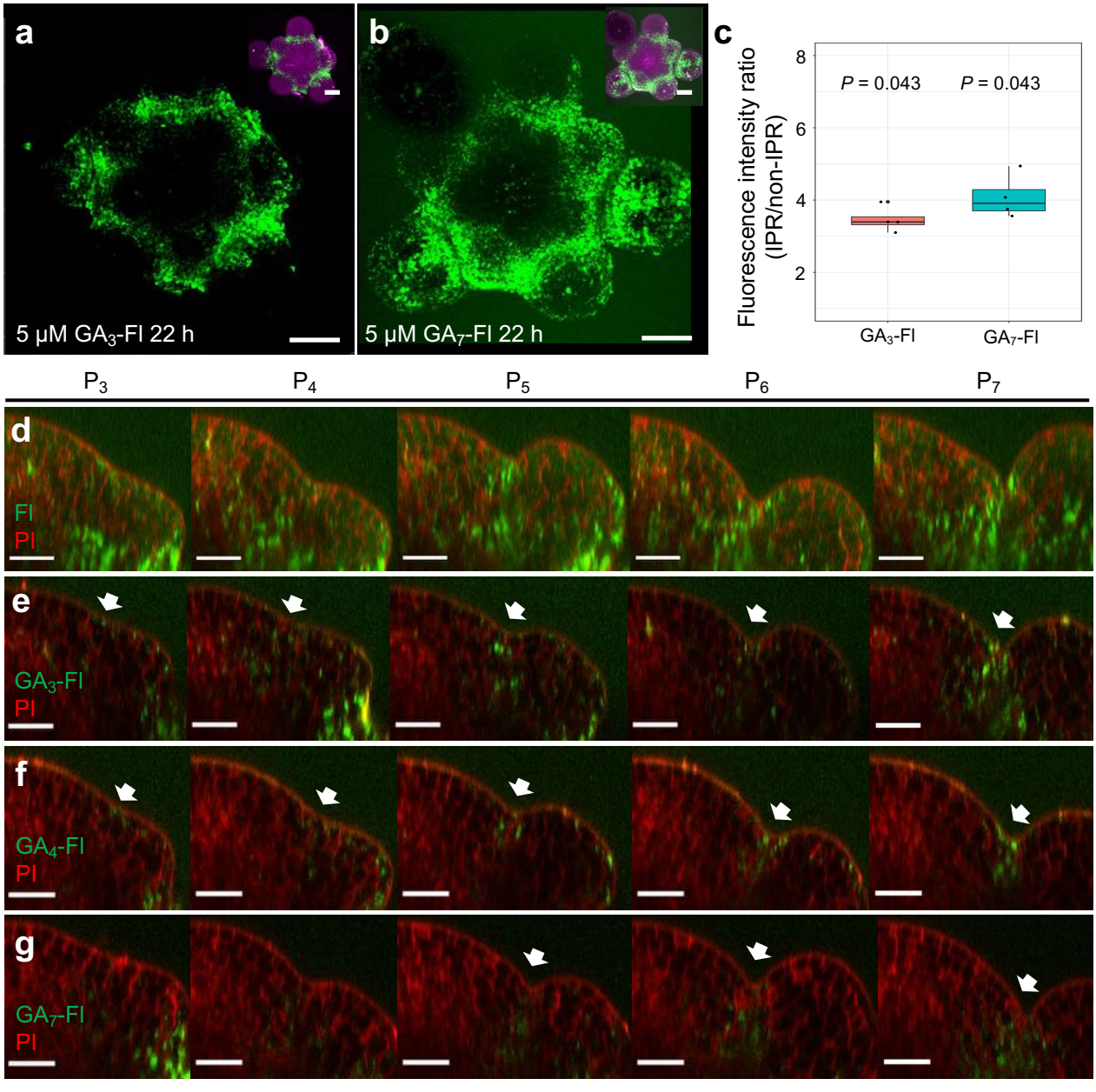

Extended data Fig. 9

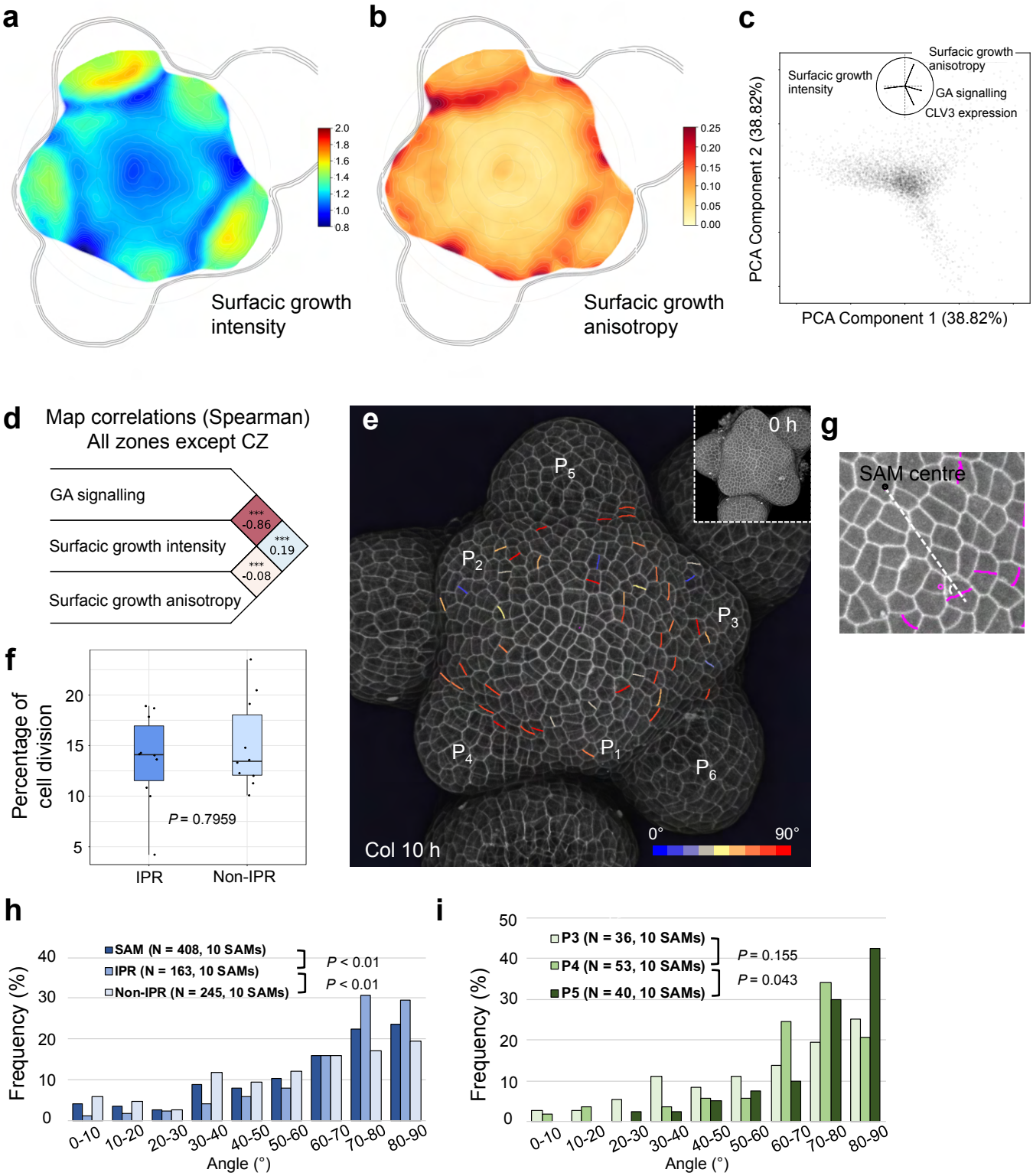
a
Surfacic growth intensity
2.0
1.8
1.6
1.4
1.2
1.0
0.8
b
Surfacic growth anisotropy
0.25
0.20
0.15
0.10
0.05
0.00
c
Surfacic growth anisotropy
Surfacic growth intensity
GA signalling
CLV3 expression
PCA Component 2 (38.82%)
PCA Component 1 (38.82%)
d
Map correlations (Spearman)
All zones except CZ
GA signalling
Surfacic growth intensity
Surfacic growth anisotropy
***
-0.86
***
0.19
***
-0.08
e
0 h
P5
P2
P3
P4
P1
P6
Col 10 h
0°
90°
g
SAM centre
f
Percentage of cell division
20
15
10
5
P = 0.7959
IPR
Non-IPR
h
Frequency (%)
SAM (N = 408, 10 SAMs)
IPR (N = 163, 10 SAMs)
Non-IPR (N = 245, 10 SAMs)
P < 0.01
P < 0.01
0-10
10-20
20-30
30-40
40-50
50-60
60-70
70-80
80-90
Angle (°)
i
Frequency (%)
P3 (N = 36, 10 SAMs)
P4 (N = 53, 10 SAMs)
P5 (N = 40, 10 SAMs)
P = 0.155
P = 0.043
Angle (°)

Fig. 5

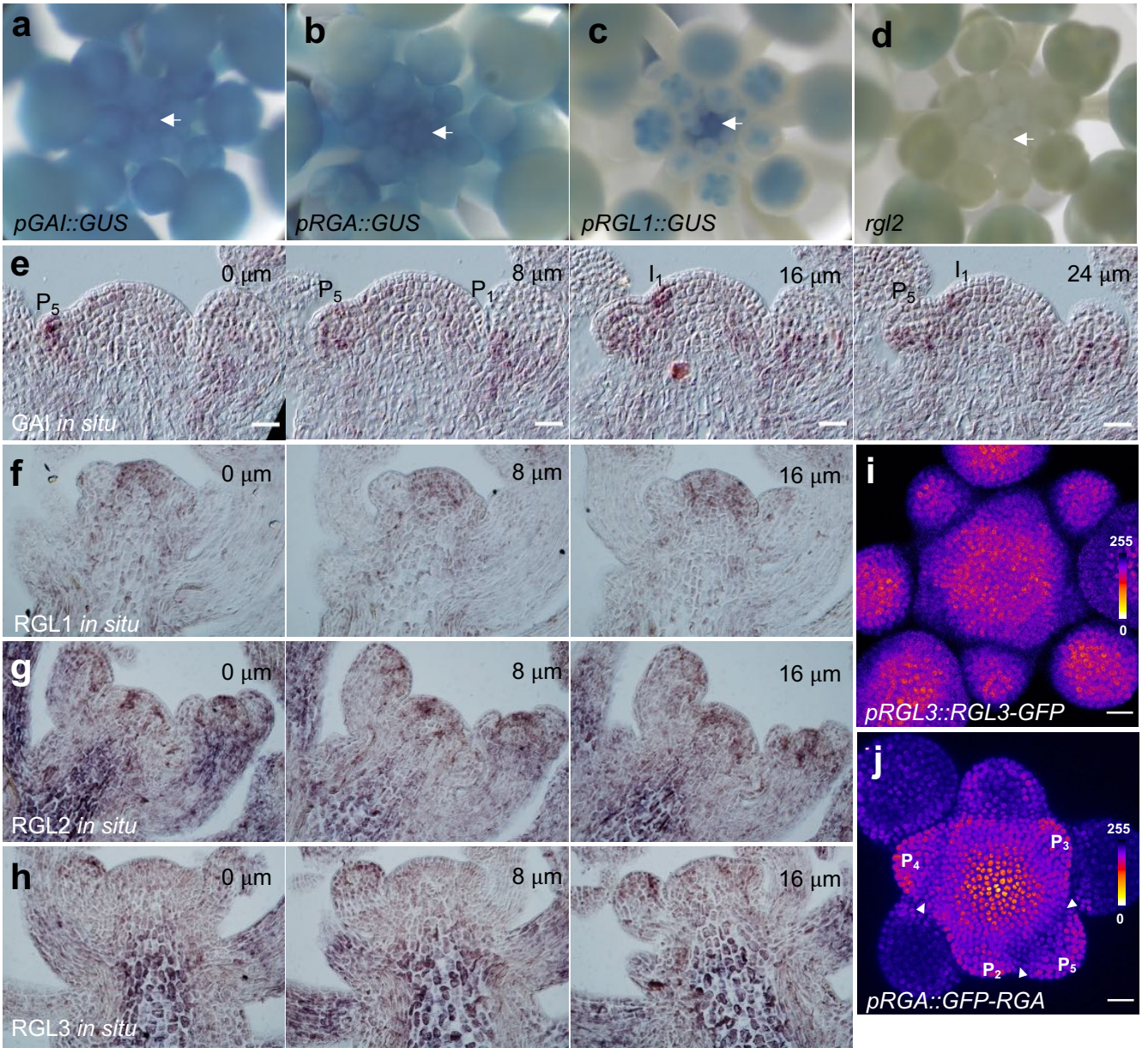

Extended Data Fig. 10

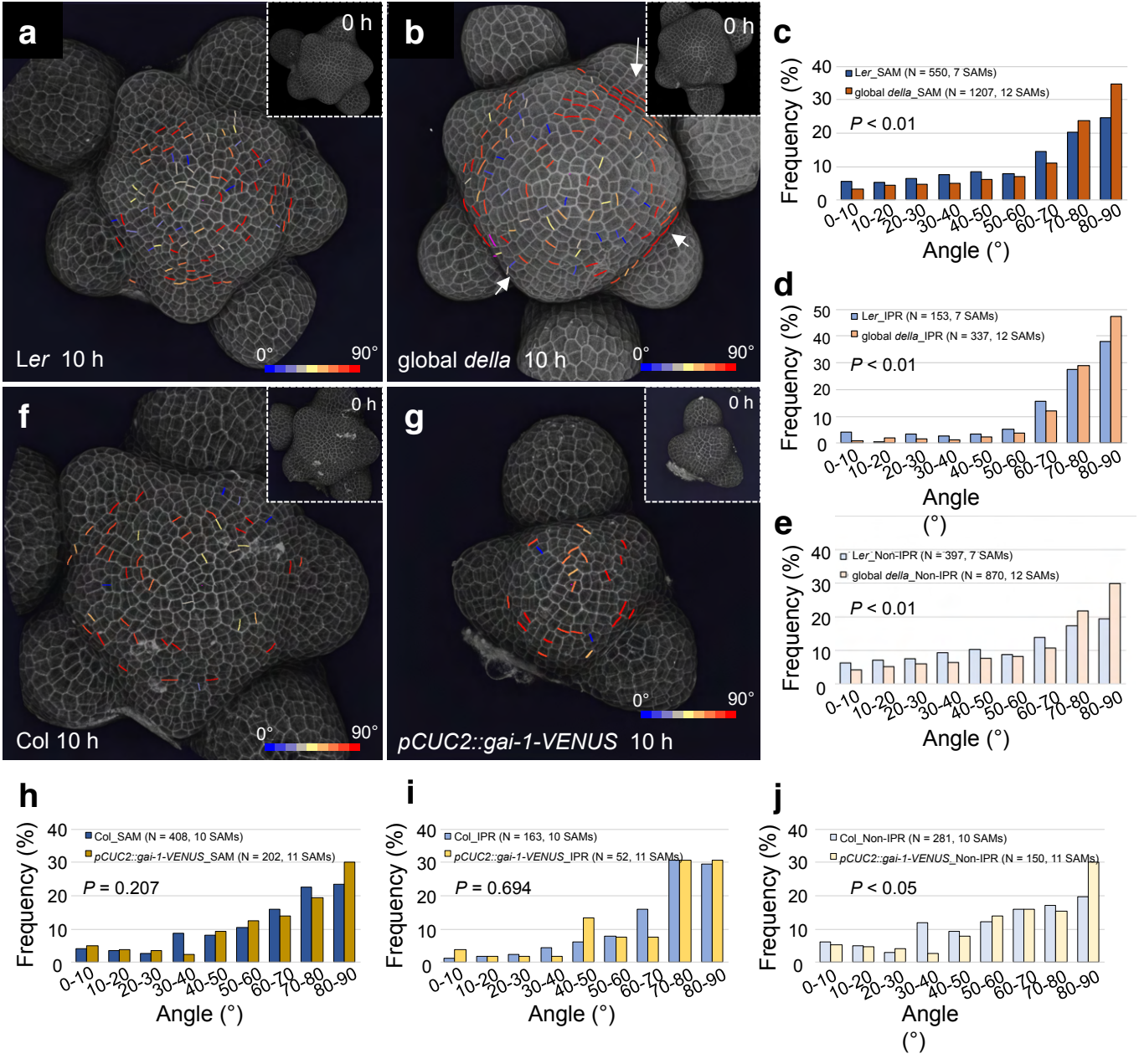
a
0 h
Ler 10 h
0°
90°
b
0 h
global della 10 h
0°
90°
c
Ler_SAM (N = 550, 7 SAMs)
global della_SAM (N = 1207, 12 SAMs)
P < 0.01
Frequency (%)
Angle (°)
d
Ler_IPR (N = 153, 7 SAMs)
global della_IPR (N = 337, 12 SAMs)
P < 0.01
Frequency (%)
Angle (°)
e
Ler_Non-IPR (N = 397, 7 SAMs)
global della_Non-IPR (N = 870, 12 SAMs)
P < 0.01
Frequency (%)
Angle (°)
f
0 h
Col 10 h
0°
90°
g
0 h
pCUC2::gai-1-VENUS 10 h
0°
90°
h
Col_SAM (N = 408, 10 SAMs)
pCUC2::gai-1-VENUS_SAM (N = 202, 11 SAMs)
P = 0.207
Frequency (%)
Angle (°)
i
Col_IPR (N = 163, 10 SAMs)
pCUC2::gai-1-VENUS_IPR (N = 52, 11 SAMs)
P = 0.694
Frequency (%)
Angle (°)
j
Col_Non-IPR (N = 281, 10 SAMs)
pCUC2::gai-1-VENUS_Non-IPR (N = 150, 11 SAMs)
P < 0.05
Frequency (%)
Angle (°)

Fig. 6

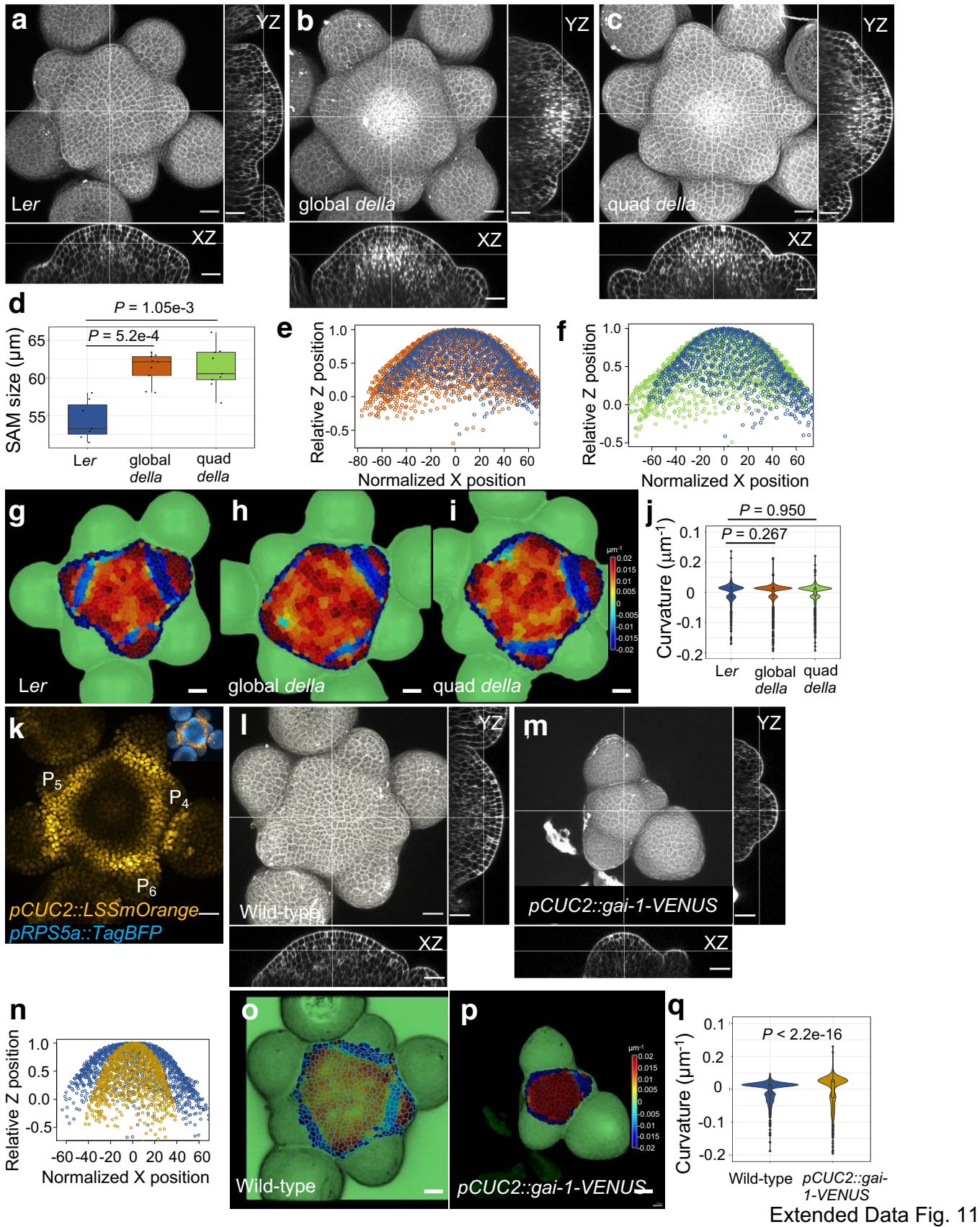

Extended Data Fig. 11

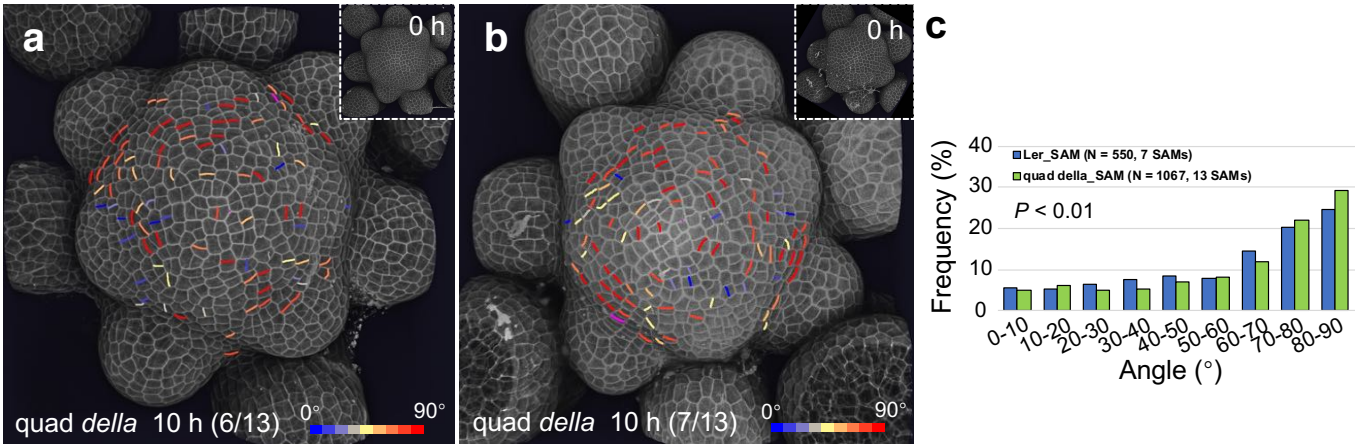

Extended Data Fig. 12

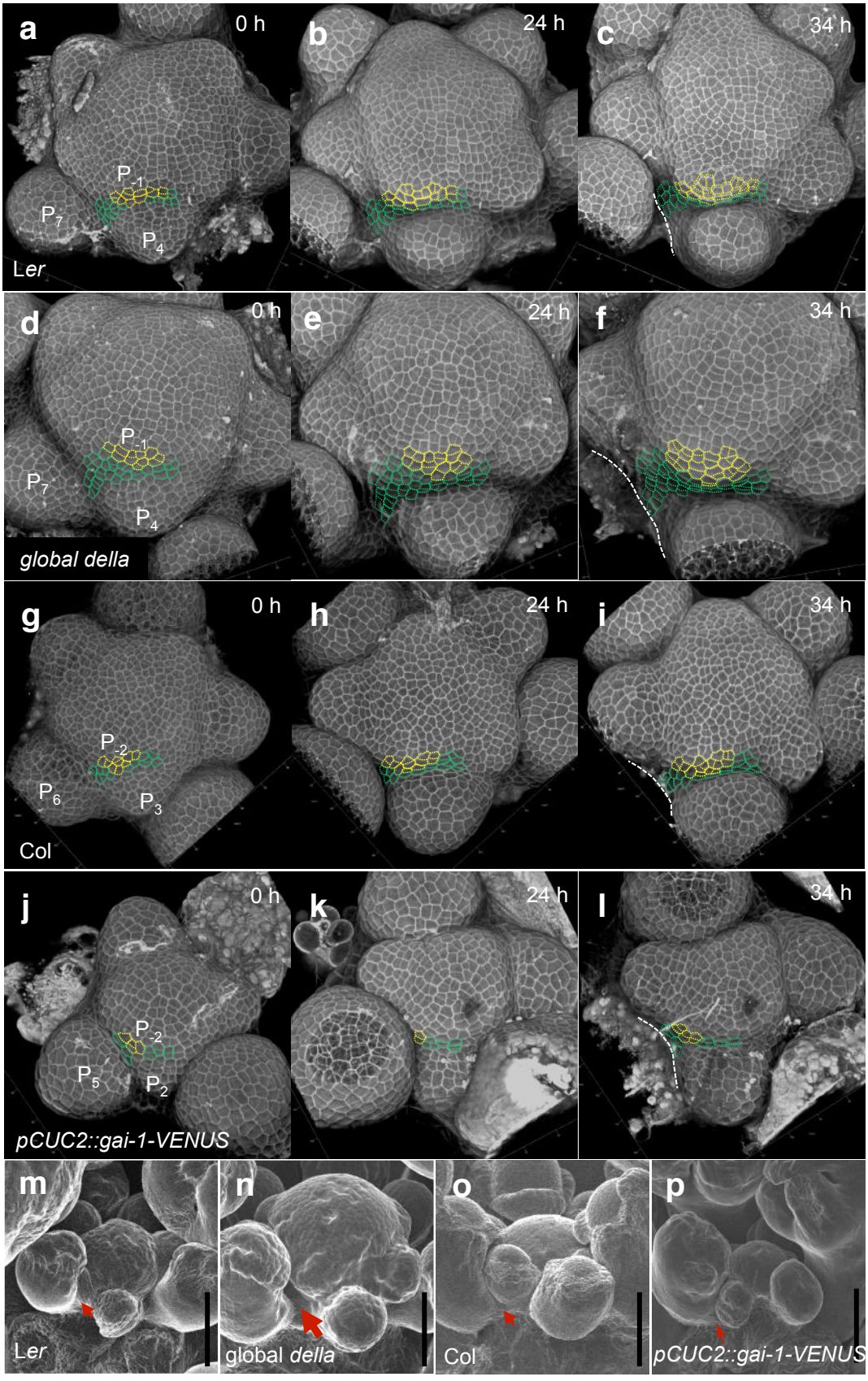
a
0 h
b
24 h
c
34 h
P-1
P7
P4
Ler
d
0 h
e
24 h
f
34 h
P-1
P7
P4
global della
g
0 h
h
24 h
i
34 h
P-2
P6
P3
Col
j
0 h
k
24 h
l
34 h
P-2
P5
P2
pCUC2::gai-1-VENUS
m
Ler
n
global della
o
Col
p
pCUC2::gai-1-VENUS

Fig. 7

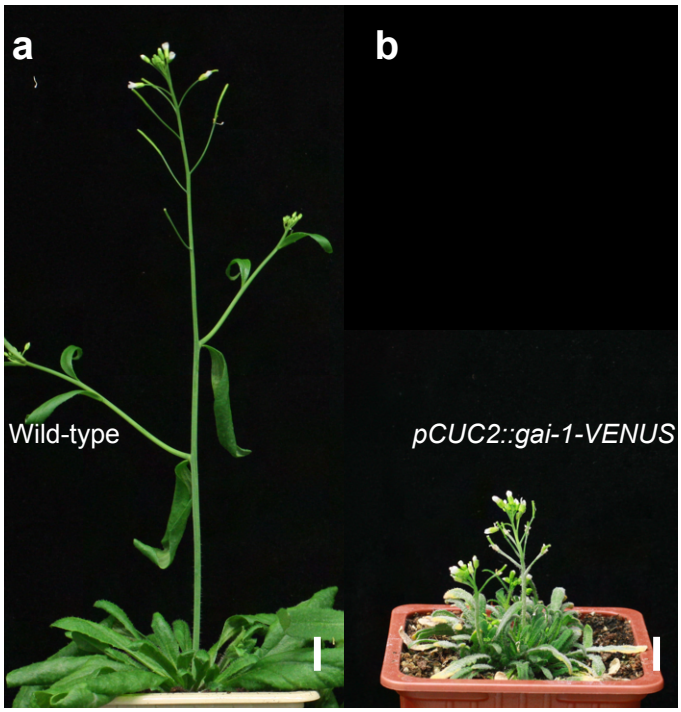

Extended Data Fig. 13

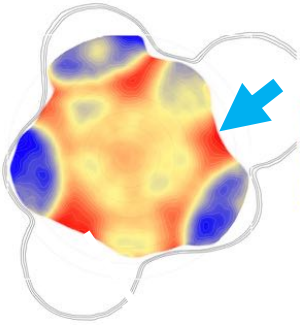

Higher GA signalling activity in the IPR

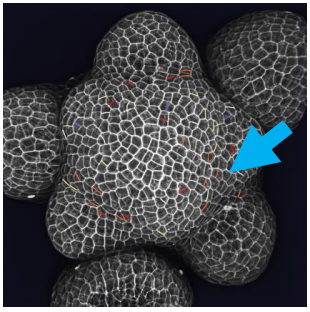

Preferential circumferential cell division orientation

Specification of the internode cellular organization

Extended Data Fig. 14